ITERATIVE FITTING APPROACH TO CR-MREPT

A THESIS SUBMITTED TO
THE GRADUATE SCHOOL OF ENGINEERING AND SCIENCE
OF BILKENT UNIVERSITY
IN PARTIAL FULFILLMENT OF THE REQUIREMENTS FOR
THE DEGREE OF
MASTER OF SCIENCE
IN
ELECTRICAL AND ELECTRONICS ENGINEERING

By
Çelik Boğa
June 2019

Iterative Fitting Approach to cr-MREPT
By Çelik Boğa
June 2019

We certify that we have read this thesis and that in our opinion it is fully adequate, in scope and in quality, as a thesis for the degree of Master of Science.

Yusuf Ziya İder(Advisor)

Nevzat Güneri Gençer

Tolga Çukur

Approved for the Graduate School of Engineering and Science:

Ezhan Karaşan
Director of the Graduate School

ABSTRACT

ITERATIVE FITTING APPROACH TO CR-MREPT

Çelik Boğa
M.S. in Electrical and Electronics Engineering
Advisor: Yusuf Ziya İder
June 2019

Electrical properties (conductivity, σ, and permittivity, ϵ) imaging, reveals information about the contrast between tissues. Magnetic Resonance Electrical Properties Tomography (MREPT) is one of the electrical properties imaging techniques, which provides conductivity and permittivity images at Larmor frequency using the perturbations in the transmit magnetic field, B_1^+. Standard-MREPT (std-MREPT) method is the simplest method for obtaining electrical properties from the B_1^+ field distribution, however it suffers from the boundary artifacts between tissue transitions. In order to eliminate this artifact, many methods are proposed. One such method is the Convection Reaction equation based MREPT (cr-MREPT). cr-MREPT method solves the boundary artifact problem, however Low Convective Field (LCF) artifact occurs in the resulting electrical property images.

In this thesis, Iterative Fitting Approach to cr-MREPT is developed for investigating the possibility of elimination of LCF artifact. In this method, forward problem of obtaining magnetic field with the given electrical properties inside the region of interest is solved iteratively and electrical properties are updated at each iteration until the difference between the solution of the forward problem and the measured magnetic field is small. Forward problem is a diffusion convection reaction partial differential equation and the solution for the magnetic field is obtained by the Finite Difference Method. By using the norm of the difference between the solution of the forward problem and the measured magnetic field, electrical properties are obtained via Gauss-Newton method. Obtaining electrical property updates at each iteration, is not a well conditioned problem therefore Tikhonov and Total Variation regularizations are implemented to solve this problem. For the realization of the Total Variation regularization, Primal Dual Interior Point Method (PDIPM) is used. Using the COMSOL Multiphysics,

simulation phantoms are modeled and B_1^+ data for each phantom is generated for electrical property reconstructions. 2D simulation phantom, modeled as an infinitely long cylindrical object, is assumed to be under the effect of the clockwise rotating radio-frequency (RF) field. Second phantom modeled, is a cylindrical object with finite length and z- independent electrical properties, that is placed in a Quadrature Birdcage Coil (QBC). Third phantom modeled is a cylindrical object placed in a QBC, with z- dependent electrical properties. In addition to the simulation phantoms, z- independent experimental phantoms are also created for MRI experiments.

Conductivity reconstructions of 2D simulation phantom, do not suffer from LCF artifact and have accurate conductivity values for both Tikhonov and Total Variation regularizations. While, 2D center slice reconstructions of the z-independent simulation and experimental phantoms do not have LCF artifact, resulting conductivity values are lower than the expected conductivity values. These low conductivity values are obtained because of the inaccurate solution of the forward problem in 2D for 3D phantoms. When Iterative Fitting Approach is extended to 3D, such that solution of the forward problem is also obtained in 3D, resulting electrical property reconstruction does not have LCF artifact and obtained conductivity values are as expected for both z- independent simulation and experimental phantom. Reconstructions obtained for the z- dependent simulation phantom shows that electrical properties varying all 3 directions can be accurately reconstructed using Iterative Fitting Approach. For Iterative Fitting Approach reconstructions, voxel size of 2 mm is used for the 3D experimental phantom and voxel size of 1.5 mm is used for all simulation phantoms and 2D experimental phantom.

Reconstructions obtained for all phantom with Iterative Fitting Approach are LCF artifact free. Conductivity reconstructions obtained using Tikhonov and Total Variation regularizations have similar resolutions (1-2 pixels) but Total Variation regularization results in smoother conductivity values inside the tissues compared to the Tikhonov regularization.

Keywords: Magnetic Resonance Imaging (MRI), Inverse Problem, Magnetic Resonance Electrical Properties Tomography (MREPT), Convection-Reaction equation based MREPT (cr-MREPT), Conductivity, Tikhonov Regularization, Total Variation Regularization.

ÖZET

KR-MREÖT İÇİN YİNELEMELİ YAKLAŞTIRMA YÖNTEMİ

Çelik Boğa
Elektrik ve Elektronik Mühendisliği, Yüksek Lisans
Tez Danışmanı: Yusuf Ziya İder
Haziran 2019

Elektriksel özellik (iletkenlik, σ, and elektriksel geçirgenlik, ϵ) görüntüleme, dokular arasında kontrast hakkında bilgiler vermektedir. Bu görüntüleme tekniklerinden birisi olan Manyetik Rezonans Elektriksel Özellik Tomografisi'nde (MREÖT), Larmor frekansında, transmit manyetik alandaki, B_1^+, bozulmalar kullanılarak iletkenlik ve elektriksel geçirgenlik görüntüleri oluşturulmaktadır. Standart-MREÖT (stt-MREÖT), B_1^+ kullanan en basit MREÖT yöntemi olmakla beraber bu yöntemle elde edilen görüntülerde dokular arası geçişlerde sınır artefaktları gözlemlenmektedir. Bu artefaktı ortadan kaldırmak amacıyla birçok yöntem önerilmiştir. Bu yöntemlerden bir tanesi Konveksiyon Reaksiyon denklemi temelli MREÖT'dir (kr-MREÖT). kr-MREÖT yöntemi sınır artefaktını ortadan kaldırmakla beraber elde edilen elektriksel özellik görüntüleri Düşük Konvektif Bölge (DKB) artefaktından etkilenmektedir.

Bu tezde, DKB artefaktının ortadan kaldırılma ihtimalini araştırmak üzere Yinelemeli Yaklaştırma Yöntemi geliştirilmiştir. Bu yöntemde, ilgilenilen bölge içerisindeki elektriksel özellikler kullanılarak manyetik alanı hesaplama ileri problemi yinelemeli olarak çözülür ve ilgilenilen bölge içerisindeki elektriksel özellikler, problemin çözümü ve ölçülen manyetik alan arasındaki fark azalana kadar güncellenir. İleri problem difüzyon konveksiyon reaksiyon kısmi diferansiyel denklemi olup, çözümü Sonlu Farklar Yöntemi ile elde edilmektedir. İleri problemin çözümü ile ölçülen manyetik alanın farkı kullanılarak, elektriksel özellikler, Gauss-Newton yöntemiyle elde edilir. Her yinelemede elektriksel özellik güncellemeleri elde etme problemi iyi koşullu bir problem olmadığı için Tikhonov ve Total Varyasyon regülarizasyonları bu problemin çözümünde kullanılmıştır. Total Varyasyon regülarizasyonu Birincil İkincil İç Nokta Yöntemi

(BİİNY) ile gerçeklenmiştir. COMSOL Multiphysics kullanılarak benzetim fantomları oluşturulmuş ve fantomlar için B_1^+ verileri oluşturulmuş ve elektriksel özellik geriçatımları kullanılmıştır. 2B benzetim fantomu, saat yönünde dönen radyo-frekans (RF) alanının etkisi altındaki, sonsuz uzunluktaki bir silindirik obje olarak modellenmiştir. Modellenen ikinci fantom, kuş kafesi sarımı içerisine yerleştirilmiş, elektrik özellikleri z- yönünde değişmeyen, sabit uzunluktaki bir silindir obje olarak modellenmiştir. Üçüncü fantom ise kuş kafesi sarımı içerisine yerleştirilmiş, elektrik özellikleri z- yönünde değişen, sabit uzunluktaki bir silindir obje olarak modellenmiştir. Benzetim fantomlarını yanısıra, deneysel fantomlar hazırlanmış ve MRG deneylerinde kullanılmıştır.

Tikhonov ve Total Varyasyon Regülarizasyonu ile elde edilen 2B benzetim fantomu iletkenlik geriçatımlarında DKB artefaktı görünmemekle birlikte iletkenlik değerleri de beklenildiği gibi bulunmaktadır. z- bağımsız deneysel ve benzetim fantomlarının 2B merkez kesit geriçatımlarında DKB artefaktı olmamakla beraber iletkenlik değerlerinin beklenen değerlerin aşağısında kaldığı gözlemlenmiştir. Bu durumun sebebi, 3B fantomların 2B ileri problem çözümünün kusurlu olmasıdır. Yinelemeli Yaklaştırma Yöntemi 3B olarak gerçeklendiğinde, ileri problemin çözümü 3B'ta elde edildiğinde, z- bağımsız benzetim ve deneysel fantomların elektriksel özellik geriçatımlarında DKB artefaktının olmadığı ve iletkenlik değerlerinin de doğru bir şekilde bulunduğu gözlemlenmiştir. z- bağımlı benzetim fantomu geriçatımlarında 3B'ta değişen iletkenlik yapılarının da Yinelemeli Yaklaştırma Yöntemi ile doğru bir şekilde görüntülenebildiği gözlemlenmiştir. Yinelemeli Yaklaştırma Yöntemi geriçatımlarında, tüm benzetim fantomları ve 2B deneysel fantom için 1.5 mm'lik, 3B deneysel fantom için 2 mm'lik vokseller kullanılmıştır.

Yinelemeli Yaklaştırma Yöntemi ile edilen elektriksel özellik gerïoatımlarında DKB artefaktı gözlemlenmemektedir. Tikhonov ve Total Varyasyon regülarizasyonları ile edilen iletkenlik geriçatımları benzer çözünürlükte olmakla beraber Total Varyasyon regülarizasyonu ile elde edilen görüntülerde dokular içi iletkenlik değerlerinin daha düz olduğu gözlenmiştir.

Anahtar sözcükler: Manyetik Rezonans Görüntüleme (MRG), Ters Problem, Manyetik Rezonans Elektriksel Özellik Tomografisi (MREÖT), Konveksiyon Reaksiyon Denklemi Temelli MREÖT (kr-MREÖT), İletkenlik, Tikhonov Regülarizasyonu, Total Varyasyon Regülarizasyonu.

Acknowledgement

I would like to express my sincere gratitude to my advisor Prof. Yusuf Ziya Ider for the continuous support of my M.Sc study and research, for his patience and immense knowledge. I am grateful for his guidance in academic field and it is been an honour working with him.

I would like to thank Prof. Nevzat Güneri Gençer and Assoc. Prof. Tolga Çukur for kindly accepting to be my jury members.

I also acknowledge The Scientic and Technological Research Council of Turkey (TUBITAK) for providing financial support, under the project code 114E522.

I would like to thank Gülşah Yıldız and Safa Özdemir for answering my questions and helping me when I needed. I would also like to thank Gökhan Arıturk, Yiğit Tuncel and Toygun Başaklar for the great office environment.

I am truly thankful to my friends, Barış Ardıç, Buğra Çevikgibi and Alp Üstün for always being on my side. Their support and advices helped me during difficult days.

Lastly, I would like to state that I am deeply grateful to my family for their endless support. Without them, it would be impossible for me to continue my studies and I am lucky to have them.

Contents

List of Figures

List of Tables

Chapter 1

Introduction

Magnetic Resonance Imaging (MRI) is an essential diagnostic tool in medicine due to the fact that it is a non-invasive imaging modality which does not use ionizing radition. MRI has many imaging parameters, hence by adjusting these parameters many contrast mechanisms can be realized. Most commonly used contrast sources are spin density and relaxation times, but there are many other contrast sources that have clinical use such as stiffness, diffusion and magnetic susceptibility. One of such contrast sources, is the electrical properties and it will be also the focus of this thesis. Electrical property imaging is benefical since it provides a contrast between benign and malignant tissues.

Use of the electrical properties and the different electrical property imaging methods will be discussed in the next section. It will be followed by the objective and scope of the thesis. In the last section, organization of the thesis will be given.

1.1 Background of Electrical Properties Imaging

Objective for the electrical property imaging is obtaining conductivity (σ) and permittivity (ϵ) of the imaged object. It has been shown that malignant tissues have increased conductivity compared to the benign tissues [1,2]. Therefore, electrical property imaging can be used as a contrast mechanism for the differentiation of the benign and malignant tissues. Moreover, electrical property imaging is also utilized in other applications such as specific absorption rate (SAR) calculation [3], hyperthermia treatment [4] and transcranical magnetic stimulation [5].

For electrical property imaging first methods introduced are electrical impedance tomography (EIT) [6, 7] and magnetic induction tomography (MIT) [8–10]. For inducing current in the imaged object, EIT method uses surface electrodes whereas MIT uses external coils. Because of the surface potentials, measurements are not very sensitive to the electrical properties at the interior regions. Hence, electrical property reconstructions obtained using EIT have low resolution at the interior regions of the imaged objects. Similarly in MIT, measured field by the external coil is not very sensitive to the electrical properties at the interior regions, leading to low resolution electrical property reconstruction at the interior regions. For solving the low resolution problem at interior regions, magnetic resonance electrical impedance tomography (MREIT) has been developed [11–16]. In this method, surface electrodes are utilized to induce currents in the frequency range of 10 Hz - 10 kHz. Then, generated magnetic field is measured by the MRI for the reconstruction of the electrical properties of the imaged object. However, when external currents below the safety limits are used in MREIT, problem of low resolution at the interior regions reoccurs.

Magnetic resonance electric properties tomography (MREPT), aims to obtain the electrical properties at the Larmor frequency, via the perturbations in the transmit radio frequency (RF) field. MREPT is introduced by Haacke (1991) [17], first successful implementation is done by Wen (2003) [18] and systematic research on the subject is started by Katscher (2009) [3].

1.2 Standard Magnetic Resonance Electrical Properties Tomography (std-MREPT)

In the most widespread formulation of MREPT [19], the electrical properties are obtained through admittivity, $\gamma = \sigma + i\omega\epsilon$. In a clock-wise rotating component of the transmitted RF magnetic field density, B_1^+, curl of both sides of Ampere's Law is taken and with the rearrangement of the terms Equation 1.1 can be obtained [19]:

$$-\nabla^2 B_1^+ = \frac{\nabla\gamma}{\gamma} \times (\nabla \times B_1^+) - i\omega\mu_0\gamma B_1^+ \tag{1.1}$$

Assumption of locally constant electrical properties, i.e. Local Homogeneity Assumption (LHA),the gradient term ($\frac{\nabla\gamma}{\gamma} \times (\nabla \times B_1^+)$), can be neglected. With this assumption 1.1 reduces to Equation 1.2, which is the standard MREPT formulation (std-MREPT). Therefore, admittivity can be obtained through Equation 1.3.

$$\nabla^2 B_1^+ = i\omega\mu_0\gamma B_1^+ \tag{1.2}$$

$$\gamma = \frac{\nabla^2 B_1^+}{i\omega\mu_0 B_1^+} \tag{1.3}$$

Despite the widespread use of standard MREPT, electrical property reconstructions obtained via Equation 1.3 suffers from the boundary artifacts due to the elimination of the gradient term in Equation 1.1. These artifacts appear at the transitions between regions with different admittivities. From the conductivity reconstruction in Figure 1.1, it can be seen that boundary artifacts are prominent at the transitions between low and high conductivity regions.

There are several approches to eliminate the boundary artifacts. Hafalir introduced convection-reaction equation based MREPT (cr-MREPT) where a partial differential equation is solved via numerical methods, in order to obtain the electrical properties [21]. In cr-MREPT, gradient term is not eliminated and electrical property reconstructions are obtained without boundary artifacts. Similarly, "gradient based Electrical Properties Tomography (gEPT)", introduced by Liu

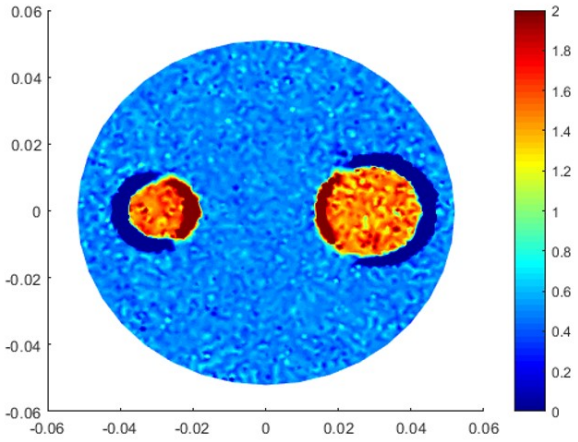

Figure 1.1: std-MREPT Conductivity Reconstruction.

has the same approach where gradient term is not eliminated. In gEPT, B_1^+ is obtained via multichannel transceiver coil and gradient of the electrical properties is obtained from this measured B_1^+ [22]. Another approach is the "Contrast Source Inversion based EPT (CSI-EPT)" where object is assumed as a scatterer placed in the field generated by the RF coil [23]. Using spatial integration starting from a seed point, electrical properties are obtained. Electrical property values are updated until the solution of integral based forward problem matches the measured B_1^+.

When both conductivity and permittivity is to be imaged, magnitude and phase of the complex B_1^+ has to be measured for the reconstruction. In order to reduce the required number of measurements and scan time, phase-based methods are introduced where only B_1^+ phase is for the conductivity reconstruction. In Equation 1.4, standard phase-based MREPT formulation is given [24]. Transcieve phase is denoted as ϕ.

$$\sigma = \frac{\nabla^2 \phi}{2\omega\mu_0} \tag{1.4}$$

Formulation given in Equation 1.4 also utilizes LHA which causes boundary artifacts in the conductivity reconstructions. To remedy this, Gurler introduced a partial differential equation based method similar to the Hafalir's method but only phase of the complex B_1^+ is used [25].

1.3 Convection Reaction Equation Based Magnetic Resonance Electrical Properties Tomography (cr-MREPT)

In convection reaction equation based MREPT (cr-MREPT), gradient term $(\frac{\nabla\gamma}{\gamma}\times(\nabla\times B_1^+))$ is not neglected. Using $\mu_0 H^+$ instead of B_1^+, x and y components of the Equation 1.1 can be written as

$$\begin{aligned}
-\nabla^2 H_x &= \frac{1}{\gamma}\left[\frac{\partial\gamma}{\partial y}\left(\frac{\partial H_y}{\partial x}-\frac{\partial H_x}{\partial y}\right)-\frac{\partial\gamma}{\partial z}\left(\frac{\partial H_z}{\partial x}-\frac{\partial H_x}{\partial z}\right)\right]-i\omega\mu_0\gamma H_x \\
-\nabla^2 H_y &= \frac{1}{\gamma}\left[\frac{\partial\gamma}{\partial z}\left(\frac{\partial H_z}{\partial y}-\frac{\partial H_y}{\partial z}\right)-\frac{\partial\gamma}{\partial x}\left(\frac{\partial H_y}{\partial x}-\frac{\partial H_x}{\partial y}\right)\right]-i\omega\mu_0\gamma H_y
\end{aligned} \tag{1.5}$$

Then, $-\nabla^2 H^+ = -\nabla^2 H_x - i\nabla^2 H_y$ is calculated and obtained as follows:

$$\begin{aligned}
-2\nabla^2 H^+ =& -i\frac{1}{\gamma}\frac{\partial\gamma}{\partial x}\left(\frac{\partial H_y}{\partial x}-\frac{\partial H_x}{\partial y}\right)+\frac{1}{\gamma}\frac{\partial\gamma}{\partial y}\left(\frac{\partial H_y}{\partial x}-\frac{\partial H_x}{\partial y}\right) \\
&-\frac{1}{\gamma}\frac{\partial\gamma}{\partial z}\left(2\frac{\partial H^+}{\partial z}-\frac{\partial H_z}{\partial x}-i\frac{\partial H_z}{\partial y}\right)-2i\omega\mu_0\gamma H^+
\end{aligned} \tag{1.6}$$

Using the fact $\nabla\cdot\vec{H}=0$, and the definition of H^+, $\left(\frac{\partial H_y}{\partial x}-\frac{\partial H_x}{\partial y}\right)$ can be obtained as in Equation 1.7.

$$\begin{aligned}
\left(\frac{\partial H_y}{\partial x}-\frac{\partial H_x}{\partial y}\right) &= \left(\frac{\partial H_y}{\partial x}-\frac{\partial H_x}{\partial y}\right)-i\left(\frac{\partial H_x}{\partial x}+\frac{\partial H_y}{\partial y}+\frac{\partial H_z}{\partial z}\right) \\
&= -2i\left(\frac{\partial H^+}{\partial x}-i\frac{\partial H^+}{\partial y}+\frac{1}{2}\frac{\partial H_z}{\partial z}\right)
\end{aligned} \tag{1.7}$$

Using the Equation 1.7, Equation 1.6 can be written as

$$\begin{aligned}
\nabla^2 H^+ =& -\frac{1}{\gamma}\frac{\partial\gamma}{\partial x}\left(\left(\frac{\partial H^+}{\partial x}-i\frac{\partial H^+}{\partial y}\right)+\frac{1}{2}\frac{\partial H_z}{\partial z}\right) \\
&-\frac{1}{\gamma}\frac{\partial\gamma}{\partial y}\left(i\left(\frac{\partial H^+}{\partial x}-i\frac{\partial H^+}{\partial y}\right)+\frac{i}{2}\frac{\partial H_z}{\partial z}\right) \\
&-\frac{1}{\gamma}\frac{\partial\gamma}{\partial z}\left[\frac{\partial H^+}{\partial z}-\frac{1}{2}\frac{\partial H_z}{\partial x}-\frac{i}{2}\frac{\partial H_z}{\partial y}\right]-i\omega\mu_0\gamma H^+
\end{aligned} \tag{1.8}$$

By defining $u = \frac{1}{\gamma}$ and multiplying Equation 1.8 with u, Equation 1.9 can be written as

$$\vec{\beta} \cdot \nabla u + \nabla^2 H^+ u - i\omega\mu_0 H^+ = 0 \tag{1.9}$$

where

$$\nabla u = \begin{bmatrix} \frac{\partial u}{\partial x} \\ \frac{\partial u}{\partial y} \\ \frac{\partial u}{\partial z} \end{bmatrix} = \begin{bmatrix} \frac{1}{\gamma^2}\frac{\partial \gamma}{\partial x} \\ \frac{1}{\gamma^2}\frac{\partial \gamma}{\partial y} \\ \frac{1}{\gamma^2}\frac{\partial \gamma}{\partial z} \end{bmatrix}, \beta = \begin{bmatrix} \frac{\partial H^+}{\partial x} - i\frac{\partial H^+}{\partial y} + \frac{1}{2}\frac{\partial H_z}{\partial z} \\ i\frac{\partial H^+}{\partial x} + \frac{\partial H^+}{\partial y} + \frac{1}{2}\frac{\partial H_z}{\partial z} \\ \frac{\partial H^+}{\partial z} - \frac{1}{2}\frac{\partial H_z}{\partial x} - \frac{i}{2}\frac{\partial H_z}{\partial y} \end{bmatrix} \tag{1.10}$$

Assuming $H_z = 0$ (valid assumption for birdcage coil) and electrical properties does not change in z-direction, $\frac{\partial u}{\partial z} = 0$, Equation 1.9 can be written in 2D form as follows

$$\vec{F} \cdot \overline{\nabla} u + \nabla^2 H^+ u - i\omega\mu_0 H^+ = 0 \tag{1.11}$$

where

$$\overline{\nabla} u = \begin{bmatrix} \frac{\partial u}{\partial x} \\ \frac{\partial u}{\partial y} \end{bmatrix}, \vec{F} = \begin{bmatrix} \frac{\partial H^+}{\partial x} - i\frac{\partial H^+}{\partial y} \\ i\frac{\partial H^+}{\partial x} + \frac{\partial H^+}{\partial y} \end{bmatrix} \tag{1.12}$$

Electrical property reconstructions obtained via cr-MREPT method are free, namely, of the boundary artifacts. However, radical changes in the reconstructed electrical properties, namely, Low Convective Field (LCF) artifact, occurs at the regions where the magnitude of the convective term, $F_x = -iF_y = \left(\frac{\partial H^+}{\partial x} - i\frac{\partial H^+}{\partial y}\right)$, is low. In Figure 1.2(a), conductivity reconstruction obtained via cr-MREPT method is shown, it can be seen that there are no boundary artifacts at the transitions regions but there is LCF artifact at the central region coinciding with the low convective field magnitude which is given in Figure 1.2(b).

In the literature, several methods have been proposed to eliminate the LCF artifact. First method is the addition of an artificial diffusion term to Equation 1.10, which was proposed by Li [26]. Objective of this method is to stabilize the numerical scheme via artificial diffusion, such that the LCF artifact is eliminated. Without noise, addition of diffusion term into the partial differential equation eliminates the LCF artifact. However, with the addition of the noise, this method cannot eliminate the LCF artifact completely. Figure 1.3 shows that without noise, addition of the artifical diffusion term eliminates the LCF artifact.

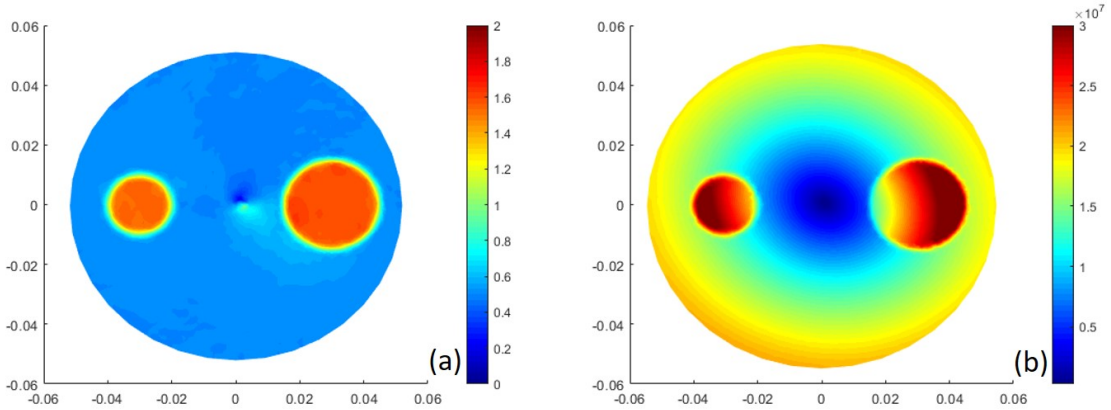

Figure 1.2: (a) cr-MREPT Conductivity Reconstruction. (b) Magnitude of the Convective Field F_x

However, with the addition of the noise LCF artifact is again prominent despite the use of artifical diffusion in cr-MREPT equation.

Ariturk proposed a method to eliminate the LCF artifact, in which multi-transmit transverse electromagnetic array is used in two different configurations. When H^+ data obtained from both configurations are used simultaneously for electrical property reconstruction, LCF artifact is eliminated in the resulting electrical property reconstructions [27]. In order to achieve this, configurations adjusted such that the LCF region in both reconstructions are non-overlapping. While this method provides LCF artifact free conductivity reconstruction using the cr-MREPT method, it requires additional TX array hardware at the MRI scanner.

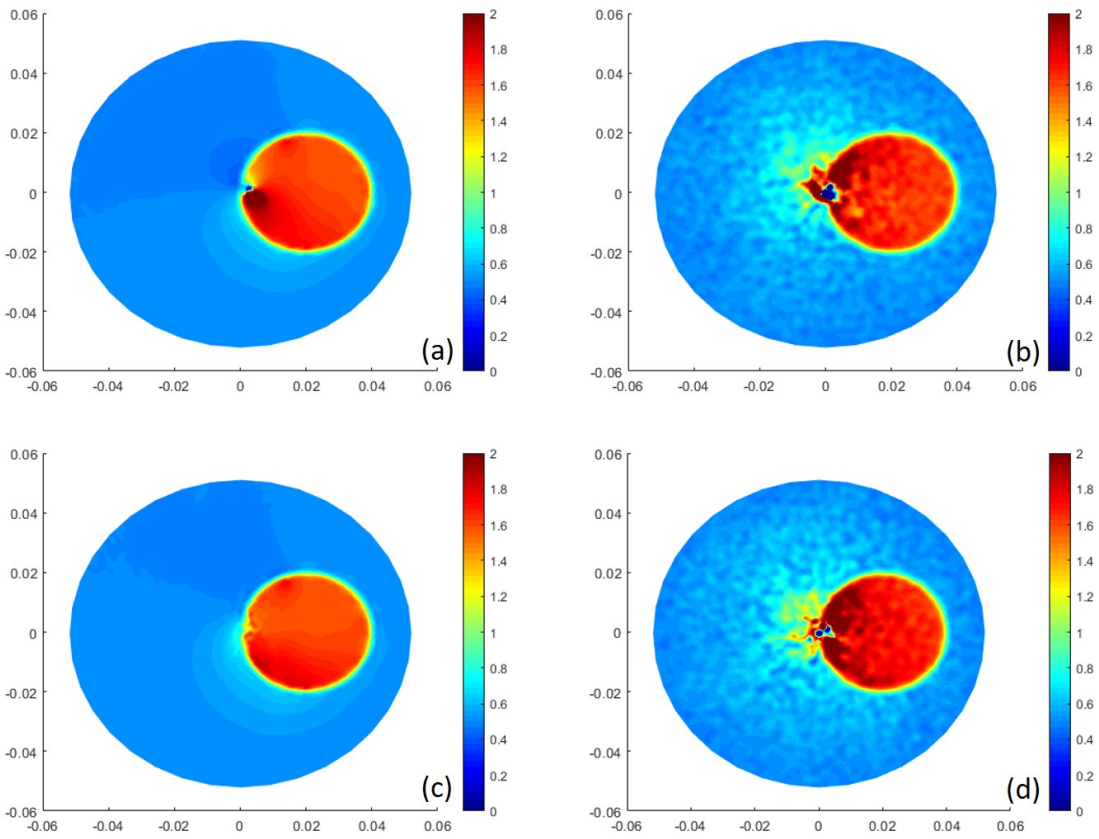

Figure 1.3: (a) cr-MREPT Conductivity Reconstruction (b) Noisy cr-MREPT Conductivity Reconstruction (c) cr-MREPT Conductivity Reconstruction with Diffusion (d) Noisy cr-MREPT Conductivity Reconstruction with Diffusion

Another method proposed by Yildiz, is to use dielectric padding near the imaged object in 2 different positions [28]. Two scans of the object is required such that position of the pad is shifted leading to a shift of LCF artifact to non-overlapping regions in each scan. Therefore, solving the cr-MREPT equation simultaneously leads to a LCF artifact free reconstruction of electrical properties. In this method LCF artifact is eliminated in the cost of increased scan time. Since position of the pad has to be changed and pad object combination has to be imaged each time, required scan time is doubled.

1.4 Objective and Scope of the Thesis

In the literature, methods are proposed for the elimanation of the LCF artifact in electrical property reconstructions obtained via cr-MREPT. However, proposed methods either require additional scan time and hardware or not robust against noise. In this thesis, Iterative Fitting Approach to cr-MREPT is developed for obtaining LCF artifact free electrical property reconstructions.

In Iterative Fitting Approach, forward problem of obtaining H^+ is solved using the electrical properties obtained at the previous iteration and electrical properties are updated at each iteration using the difference between the solution of the forward problem and the actual H^+ data.

Using the cr-MREPT equation (Equation 1.9), forward problem of obtaining a solution for H^+ inside the region of interest can be obtained as follows:

$$\begin{aligned} \vec{\theta} \cdot \nabla H^+ + u\nabla^2 H^+ - i\omega\mu_0 H^+ = 0 \\ \vec{\theta} = \left[\frac{\partial u}{\partial x} + i\frac{\partial u}{\partial y}, \frac{\partial u}{\partial y} - i\frac{\partial u}{\partial x}, \frac{\partial u}{\partial z}\right]^T \end{aligned} \tag{1.13}$$

The uniqueness theorem proved by Ammari in 2015 [29], states that if the electrical properties inside the region of interest along with the H^+ at the region boundaries are known, H^+ inside the region of interest can be accurately calculated. This theorem shows that solution of the forward problem is accurate for the electrical property distribution at each iteration.

Instead of using the 3D cr-MREPT equation, using the 2D cr-MREPT equation (Equation 1.11) forward problem for 2D can be obtained as follows.

$$\begin{aligned} \vec{\theta} \cdot \overline{\nabla} H^+ + u\nabla^2 H^+ - i\omega\mu_0 H^+ = 0 \\ \vec{\theta} = \left[\frac{\partial u}{\partial x} + i\frac{\partial u}{\partial y}, \frac{\partial u}{\partial y} - i\frac{\partial u}{\partial x}\right]^T \end{aligned} \tag{1.14}$$

After solving the forward problem, electrical property updates are obtained by minimizing the norm between solution of the forward problem and the actual

H^+ data. Obtaining the electrical propety updates at each iteration is an ill-conditioned problem, which is a common case for inverse problems. In order to overcome this ill-condition, Tikhonov and Total Variation regularizations are used with Iterative Fitting Approach. 2D and 3D electrical property reconstructions are obtained via Iterative Fitting Approach with Tikhonov and Total Variation regularizations for simulation and experimental phantoms.

1.5 Organization of the Thesis

This thesis has 4 chapters.

In Chapter 2, the developed method for LCF artifact elimination, Iterative Fitting Approach is elucidated. Mathematical background for the method is presented: forward problem formulation, solution of the forward problem, solution for electrical properties using the aforementioned forward problem and implementation of the Tikhonov and Total Variation regularization are discussed. Necessity of the 3D extension of the Iterative Fitting Approach is discussed. Simulation and experimental methods used for magnetic field data generation and measurement, are explained.

In Chapter 3, results for accuracy of the forward problem solution is presented along with the results for 2D and 3D implementation of the Iterative Fitting Approach with Tikhonov and Total Variation regularizations.

In Chapter 4, concluding remarks are stated along with the summary of the Iterative Fitting Approach method. Possible future work in implementation and realization of the Iterative Fitting Approach is discussed.

Chapter 2

Theory and Methods

2.1 Iterative Fitting Approach to cr-MREPT

2.1.1 Forward Problem Formulation

In cr-MREPT method, electrical property reconstructions are obtained by solving Equations 1.9 and 1.11 inside a region of interest (ROI).

$$\begin{aligned} \vec{\beta} \cdot \nabla u + \nabla^2 H^+ u - i\omega\mu_0 H^+ &= 0 \\ \vec{\beta} = \left[\frac{\partial H^+}{\partial x} - i\frac{\partial H^+}{\partial y},\ i\frac{\partial H^+}{\partial x} + \frac{\partial H^+}{\partial y}, \frac{\partial H^+}{\partial z} \right]^T & \end{aligned} \tag{2.1}$$

Equation 2.1 is the cr-MREPT partial differential equation where $u = \frac{1}{\gamma}$ and coefficients are obtained from H^+ and its derivatives. This is the inverse problem formulation for obtaining the electrical property reconstructions. It is also an implicit solution of electrical property reconstructions.

Using the cr-MREPT equation, forward problem of calculating H^+ data inside the region of interest using the electrical properties inside the region is obtained as follows.

$$\begin{aligned} \vec{\theta} \cdot \nabla H^+ + u\nabla^2 H^+ - i\omega\mu_0 H^+ = 0 \\ \vec{\theta} = \left[\frac{\partial u}{\partial x} + i\frac{\partial u}{\partial y},\ \frac{\partial u}{\partial y} - i\frac{\partial u}{\partial x}, \frac{\partial u}{\partial z}\right]^T \end{aligned} \tag{2.2}$$

Forward problem is also a partial differential equation but unknowns are the H^+ values and coefficients are calculated using electrical properties, u. Using this formulation, electrical property reconstructions are obtained via an iterative method with two steps. First, forward problem is solved to calculate H^+ inside the ROI using the electrical property values from the previous iteration. For the first iteration, uniform distribution of the electrical properties is used. Then, electrical property values are updated using the difference between calculated H^+ and measured H^+. When calculated H^+ values and measured H^+ values become close, electrical properties inside the region of interest will be obtained. This method is called "Iterative Fitting Approach (IFA)".

Iterative Fitting Approach is realizable because of the uniqueness theorem proved by Ammari, in 2015 [29].Without this theorem, H^+ calculation, had to be done for the entire 3D space at the first step and electrical property updates would be calculated for the entire 3D space. However, using this theorem, Iterative Fitting Approach can be realized for the region of interest inside the imaged object.

Iterative Fitting Approach can also be realized in 2D space as well as 3D space with using the 2D cr-MREPT equation for a single slice. If electrical properties are assumed to be translationally uniform in the z- direction, corresponding forward problem in 2D form can be written as in Equation 2.3. This forward problem formulation was provided previously but it has been provided again for emphasizing the 2D formulation before continuing to following sections. In this

formulation, $\overline{\nabla} = [\frac{\partial}{\partial x}, \frac{\partial}{\partial y}]^T$ is the 2 dimensional gradient operator.

$$\begin{aligned} \vec{\theta} \cdot \overline{\nabla} H^+ + u\nabla^2 H^+ - i\omega\mu_0 H^+ = 0 \\ \vec{\theta} = \left[\frac{\partial u}{\partial x} + i\frac{\partial u}{\partial y},\ \frac{\partial u}{\partial y} - i\frac{\partial u}{\partial x}\right]^T \end{aligned} \tag{2.3}$$

In Chapter 3, results for the solution of the forward problem is provided. It can be seen that H^+ can be calculated accurately using the actual electrical properties inside the desired region which falls inline with the Ammari's uniqueness theorem.

2.1.2 Discretization of the Forward problem

In general forward problem, Equation 2.3, does not have an analytical solution. Therefore, H^+ inside the region of interest is calculated using numerical methods. In the Iterative Fitting Approach, Finite Difference Method is used on a uniform grid to solve the forward problem.

H^+ values and the electrical properties on the nodes of this uniform grid is denoted as H and U respectively. Using the central difference formulas, derivatives in x- and y- directions ($\frac{\partial}{\partial x}$ and $\frac{\partial}{\partial y}$) and the Laplacian ($\nabla^2$) operator matrices are constructed. Derivative operator matrices in x- and y- direction on the nodes of the uniform grid, are denoted as $\mathbf{D_x}$ and $\mathbf{D_y}$ respectively. Laplacian operator matrix is denoted as $\mathbf{D_2}$. Finite Difference Method is used for the operator matrix construction are as follows.

$$\begin{aligned} \frac{\partial u_{i,j}}{\partial x} = \frac{u_{i+1,j} - u_{i-1,j}}{2dx}, \frac{\partial^2 u_{i,j}}{\partial x^2} = \frac{u_{i+1,j} - 2u_{i,j} + u_{i-1,j}}{dx^2} \\ \frac{\partial u_{i,j}}{\partial y} = \frac{u_{i,j+1} - u_{i,j-1}}{2dy}, \frac{\partial^2 u_{i,j}}{\partial y^2} = \frac{u_{i,j+1} - 2u_{i,j} + u_{i,j}}{dy^2} \end{aligned} \tag{2.4}$$

Then, using these operator matrices, partial differential equation of forward problem is converted to a set of linear equations in the form of $AH = 0$. Formulation of the coeffecient matrix $\mathbf{A}$, using the discrete operator matrices and the

electrical properties, is given in Equation 2.5.

$$\mathbf{A} = diag[(\mathbf{D_x} - i\mathbf{D_y})U]D_x + diag[(\mathbf{D_y} - i\mathbf{D_x})U]D_y + diag[U]\mathbf{D_2} - i\omega\mu_0\mathbf{I} \quad (2.5)$$

$diag[]$ operator converts a $N \times 1$ vector into a $N \times N$ matrix with diagonal entries are the vector itself (i^{th} diagonal entry of the matrix is the i^{th} element of the vector) and other entries are equal to zero. It can be seen that coefficient matrix $\mathbf{A}$ is dependent on the electrical properties and their derivatives.

$\mathbf{A}$ matrix and H vector partitioned with respect to inner and boundary nodes resulting in $\mathbf{A_{in}}H_{in} = -\mathbf{A_{boun}}H_{boun} = b$. Unknown H^+ values at the inner nodes are denoted as H_{in} and H_{boun} denotes the H^+ values at the boundary nodes. H_{boun} values are selected as the measured H^+ values at the same boundary nodes for satisfying the condition for the Ammari's uniqueness theorem.

2.1.3 Solution for Electrical Properties

In order to obtain the solution for electrical properties, conductivity (σ) and permittivity (ϵ), the L_2 norm between the calculated H^+ values from the forward problem (denoted as H^c_{in} at the inner nodes) and the measured H^+ values (denoted as H^m_{in} at the inner nodes) has to be minimized. This leads to the minimization problem given in Equation 2.6.

$$\min \ ||H^c_{in} - H^m_{in}||_2^2 \quad (2.6)$$

Using the Taylor series expansion, solution of the forward problem at the inner nodes, H^c_{in}, can be written as follows

$$H^c_{in} = H^0_{in} + \frac{\partial H^c_{in}}{\partial U}\bigg|_{U_0,H^0_{in}}(U - U_0) + \frac{1}{2}\frac{\partial^2 H^c_{in}}{\partial U^2}\bigg|_{U_0,H^0_{in}}(U - U_0)^2 + \dots \quad (2.7)$$

In Equation 2.7, H^0_{in} and U_0 are the calculated H_{in} and U values from the previous iteration. $\frac{\partial H^c_{in}}{\partial U}\big|_{U_0,H^0_{in}}$ term is the Jacobian matrix and it will be denoted

as $\mathbf{S}$. Electrical property updates, ΔU, will be defined as $\Delta U = U - U_0$. Therefore, by ignoring the higher order terms, H_{in}^c can be modeled as follows.

$$H_{in}^c = H_{in}^0 + \mathbf{S}\Delta U \tag{2.8}$$

Then inserting Equation 2.8 into Equation 2.6, Equation 2.9 can be obtained as follows

$$\min \ ||H_{in}^0 - H_{in}^m + \mathbf{S}\Delta U||_2^2 \tag{2.9}$$

Electrical property updates, ΔU, can be obtained via the solution of the minimization problem given in Equation 2.9 at each iteration until the solution of the forward problem, H_{in}^c and the measued H^+ data are close.

For solving the minimization problem, real and imaginary parts of the ΔU are seperated such that Equation 2.9 transformed to Equation 2.10. Where new Jacobian matrix is generated by using the fact that Jacobian matrix for imaginary part of ΔU is Jacobian matrix for real part of ΔU multiplied with i. Subcript r denotes the real part and subscript i denotes the imaginary part.

$$\left|\left| \begin{bmatrix} H_{in,r}^0 \\ H_{in,i}^0 \end{bmatrix} - \begin{bmatrix} H_{in,r}^m \\ H_{in,i}^m \end{bmatrix} + \begin{bmatrix} \mathbf{S_r} & -\mathbf{S_i} \\ \mathbf{S_i} & \mathbf{S_r} \end{bmatrix} \begin{bmatrix} \Delta U_r \\ \Delta U_i \end{bmatrix} \right|\right|_2^2 \tag{2.10}$$

2.1.4 Calculation of Jacobian Matrix

At each iteration of Iterative Fitting Approach method, Jacobian matrix S has to be calculated. Due to the lack of analytical relation between electrical properties and the coefficient matrix $\mathbf{A}$, Jacobian matrix $\mathbf{S}$ is calculated using numerical methods. Equation 2.11 shows the formulation of the Jacobian matrix for N inner nodes.

$$\mathbf{S} = [\frac{\partial H_{in}}{\partial u_1} \cdots \frac{\partial H_{in}}{\partial u_N}] \tag{2.11}$$

2.1.4.1 Finite Difference Based Method

First calculation method for the **S** matrix is the Finite Difference Based method. In Finite Difference Based method an element of U, that belongs to inner nodes, is increased slightly and using this new U vector, forward problem is solved. Then, using forward differencing column of the **S** matrix corresponding to that index will be calculated. Repeating this procedure for all inner nodes, **S** matrix will be calculated.

However, this method requires a long computation time due to the fact that for each inner node solution of a linear system has to be calculated, i.e. matrix inversion is calculated at each step. Due to the immense number of inner nodes, calculating **S** matrix with this method results in long iteration times. Hence, using the Finite Difference based method significantly increases required time for the electrical property reconstructions.

2.1.4.2 Semi-Analytic Method

In order to reduce the computation time for the calculation of **S** matrix, semi-analytic method is developed. Total differential of the forward problem, $\mathbf{A_{in}}H_{in} = b$, for a interior point can be obtained as in Equation 2.12.

$$\frac{\partial \mathbf{A}}{\partial u_i} H_{in}^0 + \mathbf{A_0} \frac{\partial H_{in}}{\partial u_i} = \frac{\partial b}{\partial u_i} \tag{2.12}$$

H_{in}^0 is the solution of the forward problem, calculated H_{in}, for that iteration, $\mathbf{A_0}$ is the coeffient matrix used for the solution of the forward problem and u_i is the electrical property value at inner node i. And by rearranging the terms Equation 2.12 can be written as follows.

$$\frac{\partial H_{in}}{\partial u_i} = \mathbf{A_0}^{-1} \left[\frac{\partial b}{\partial u_i} - \frac{\partial \mathbf{A}}{\partial u_i} H_{in}^0 \right] \tag{2.13}$$

Using Equation 2.13, each corresponding column of **S** matrix can be calculated for each u_i until the **S** matrix is completed. However, $\frac{\partial \mathbf{A}}{\partial u_i}$ and $\frac{\partial b}{\partial u_i}$ cannot

be calculated analytically but using Equation 2.5 and index information of the finite difference operator matrices, they can be calculated numerically. Defining $\mathbf{B_i} = \frac{\partial b}{\partial u_i} - \frac{\partial \mathbf{A}}{\partial u_i} H^0_{in}$, for each inner node and taking common term $\mathbf{A_0^{-1}}$ out of the paranthesis, Equation 2.11 can be written as follows.

$$\mathbf{S} = \mathbf{A_0^{-1}} \big[B_1 \dots B_N \big] \tag{2.14}$$

With Equation 2.14, Jacobian matrix $\mathbf{S}$ can be calculated using a single linear system of equation solution. Whereas finite difference based method requires N linear system of equation solution. Therefore, semi-analytic calculation method is significantly faster and computationally efficient. For example, for 3925 inner node, $\mathbf{S}$ matrix is calculated in 14 seconds with the semi-analytic method, where using finite difference based calculation method $\mathbf{S}$ matrix takes 255 seconds. Which indicates that using the developed semi-analytic method, reduces the required computation time for each iteration and for overall electrical property reconstruction.

2.1.5 Regularization

Using the definition $H^+ = \frac{1}{2}(H_x + iH_y)$, $F_x = (\frac{\partial H^+}{\partial x} - i\frac{\partial H^+}{\partial y})$ term in Equation 1.11 can be written as follows:

$$F_x = \frac{\partial H_x}{\partial x} + \frac{\partial H_y}{\partial y} + i(\frac{\partial H_y}{\partial x} - \frac{\partial H_x}{\partial y}) \tag{2.15}$$

Using the fact that $\nabla \dot{H} = 0$ and assuming $\frac{\partial H_z}{\partial z}$, Equation 2.15 can be simplified to $F_x \cong \frac{i}{2}(\frac{\partial H_y}{\partial x} - \frac{\partial H_x}{\partial y})$. Then by using the z- component of the Ampere's Law, Equation 2.16 can be obtained [27].

$$2iF_x = \gamma E_z \tag{2.16}$$

Equation 2.16, shows that magnitude of the convective field, F_x, is directly related to the electric field, E_z. In the regions where magnitude of the F_x is close

to 0, magnitude of the E_z is also close to 0. This indicates an insensitivity to the γ values for the regions with low F_x magnitude therefore in the solution of the forward problem. This creates an ill-condition in the problem for obtaining the electrical property updates at each iteration.

Singular value decomposion of the real and imaginary separated $\mathbf{S}$ matrix is calculated, where matrix $\mathbf{V}$ consists of right singular vectors, which are the basis functions of the solution space. In Figure 2.1(a-p), magnitude of the images obtained from the columns of $\mathbf{V}$ are shown for the singular values number $1, 10, 30, 50, 100, 200, 500, 1000, 3000, 5000, 7000, 7500, 7600, 7700, 7800$ and 7850. Where largest singular value is number 1 is and the smallest singular values is number 7820. Figure 2.2, shows the normalized singular value decomposition for real and imaginary seperated $\mathbf{S}$ matrix is given.

Figures 2.1 and 2.2, shows that small singular values correspond to the basis functions relating the electrical property updates at the region where magnitude of the F_x. Which indicates that there is in ill-condition for obtaining the electrical property updates, arising from the insensitivity to the electrical property values at the LCF region.

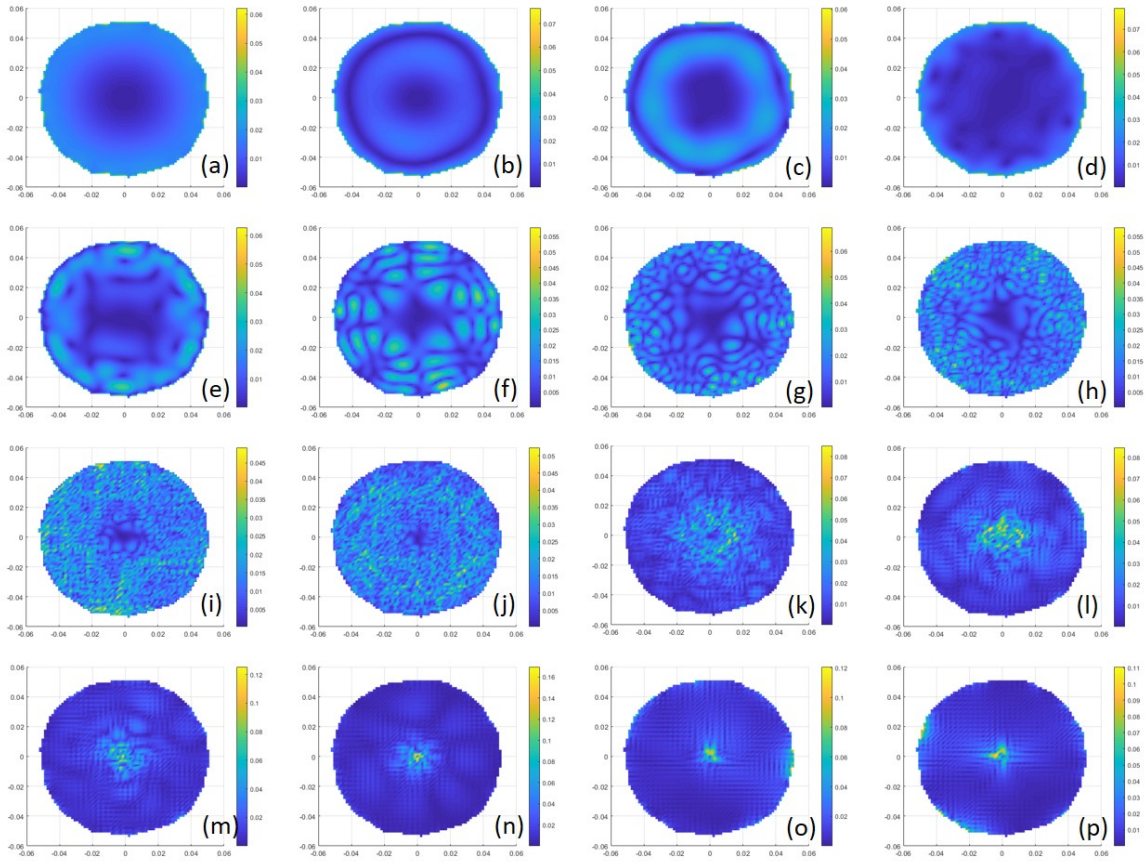

Figure 2.1: (a-p) Magnitude of the Images Obtained from the Columns of $\mathbf{V}$ for the Singular Values number $1, 10, 30, 50, 100, 200, 500, 1000, 3000, 5000, 7000, 7500, 7600, 7700, 7800$ and 7850

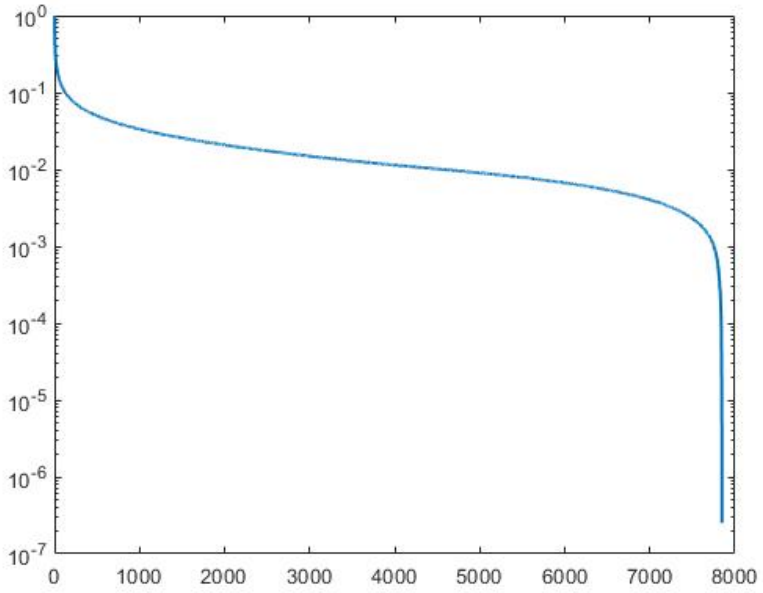

Figure 2.2: Normalized Singular Value Decomposition for Real and Imaginary Seperated S Matrix

Due to the ill-conditioned nature of the problem, electrical property updates cannot be obtained directly from the minimization problem given in Equation 2.10. In Figure 2.2, normalized singular values of the **S** matrix, for 3925 inner nodes (real and imaginary parts are seperated), with respect to the largest singular value is given where the condtion number, value of the lowest singular value, indicates that Equation 2.10 is an ill-conditioned problem.

In order to obtain a solution for ΔU, regularization terms are added to the minimization problem. With the addition of the regularization term, ill-condition of the problem is reduced such that solution for ΔU can be obtained. Moreover, with the application of the regularization to Equation 2.10, artifacts in the electrical property reconstructions such as boundary and LCF artifacts will also be eliminated. Tikhonov and Total Variation Regularization is used for reconstructions with Iterative Fitting Approach.

2.1.5.1 Tikhonov Regularization

First regularization used in Iterative Fitting Approach is the Tikhonov regularization. In order to realize this regularization, $||\Delta U||_2^2$ term is added to the minimization problem given in Equation 2.9, with regularization parameter λ. Resulting minimization problem is as follows.

$$||H_{in}^0 - H_{in}^m + \mathbf{S}\Delta U||_2^2 + \lambda||\Delta U||_2^2 \tag{2.17}$$

Equation 2.17 is a quadratic problem and solution of ΔU in the least squares sense is obtained as

$$\Delta U = (\mathbf{S}^T\mathbf{S} + \lambda\mathbf{I})^{-1}(\mathbf{S}^T(H_{in}^0 - H_{in}^m)) \tag{2.18}$$

When real and imaginary parts of the electrical property updates, ΔU's, are seperated Equation 2.17 is transformed into Equation 2.19.

$$\left|\left|\begin{bmatrix} H_{in,r}^0 \\ H_{in,i}^0 \end{bmatrix} - \begin{bmatrix} H_{in,r}^m \\ H_{in,i}^m \end{bmatrix} + \begin{bmatrix} \mathbf{S_r} & -\mathbf{S_i} \\ \mathbf{S_i} & \mathbf{S_r} \end{bmatrix} \begin{bmatrix} \Delta U_r \\ \Delta U_i \end{bmatrix}\right|\right|_2^2 + \left|\left|\begin{bmatrix} \Delta U_r \\ \Delta U_i \end{bmatrix}\right|\right|_2^2 \tag{2.19}$$

With the implementation of Tikhonov regularization, ill-condition of the problem is reduced due to the fact that lowest singular value has a lower limit due the $||\Delta U||_2^2$ term. Limit itself is related to the regularization parameter λ. In figure 2.3, normalized singular values for the coefficient matrix of Equation 2.19 is given and it can be seen that condition number of the problem is reduced.

2.1.5.2 Total Variation Regularization

In general, Tikhonov regularization results in smoother transitions between different regions, whereas Total Variation regularization results in sharper transitions [30, 31]. Therefore, for obtaining sharper transitions between tissues, Total Variation regularization is also implemented with Iterative Fitting Approach. For the realization of Total Variation regularization, $\int_\Omega |\nabla U| d\Omega$ term is added to the

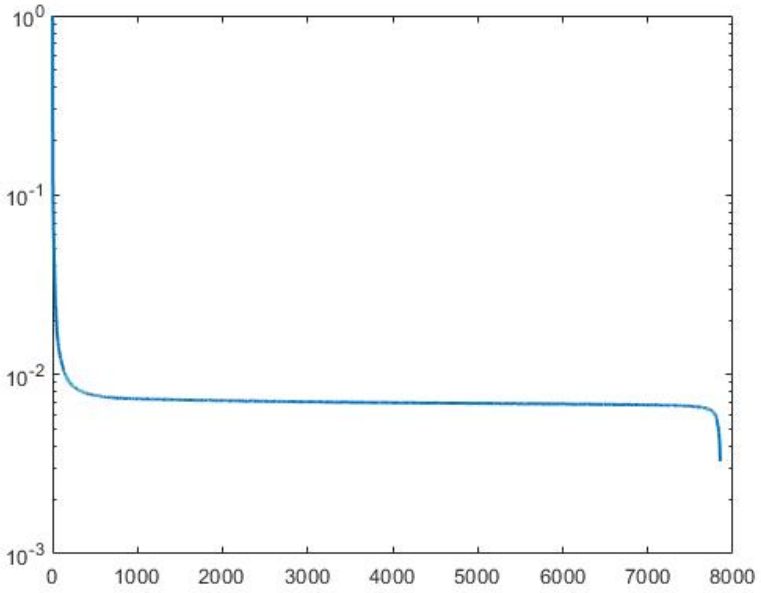

Figure 2.3: Normalized Singular Value Decomposition for Real and Imaginary Seperated **S** Matrix with Tikhonov Regularization with $\lambda = 0.005$

minimization problem given in Equation 2.9. Resulting minimization problem is given in Equation 2.20 and β is the regularization parameter.

$$||H_{in}^0 - H_{in}^m + \mathbf{S}\Delta U||_2^2 + \beta \int_\Omega |\nabla U| d\Omega \tag{2.20}$$

Total Variation regularization term, $\int_\Omega |\nabla U| d\Omega$, is not differentiable due to the L_1 norm, hence, the solution of the Equation 2.20 can only be obtained via approximations of it's derivative [31, 32]. Primal Dual Interior Point Method (PDIPM) is used for the implementation of the Total Variation regularization since this method is previously used for MREIT [33] and std-MREPT [34] conductivity reconstructions.

2.1.5.3 Primal Dual Interior Point Method (PDIPM)

In the PDIPM, the Total Variation term is discretized for each index and resulting in $\sum_i |L_i U|$, where L_i is i^{th} row of the summation of derivative operator matrices in x- and y- directions ($\mathbf{L}$ matrix). Total Variation regularized problem formulation with discretized Total Variation term, given in Equation 2.21, is labeled as the primal problem.

$$\arg\min_{U} ||H_{in}^0 - H_{in}^m + \mathbf{S}\Delta U||_2^2 + \beta \sum_i |L_i U| \tag{2.21}$$

Then, by defining auxilary variables χ, for each index i, L_1 norm can be written as follows.

$$|L_i U| = \max_{\chi_i, |\chi_i| \leq 1} \chi_i L_i U \tag{2.22}$$

By inserting Equation 2.22 into the primal problem, Equation 2.21, a second equivalent problem is obtained as in Equation 2.23. This is the dual problem and auxilary variables χ's are the dual variables.

$$\max_{\chi_i, |\chi_i| \leq 1} \arg\min_{U} ||H_{in}^0 - H_{in}^m + \mathbf{S}\Delta U||_2^2 + \beta \sum_i \chi_i L_i U \tag{2.23}$$

For the feasible points where $|\chi_i| < 1$, cost function of primal problem (Equation 2.21) takes larger values than the cost function of the dual problem (Equation 2.23). But both cost functions take the same value at a single point, which is the optimal point for both functions. This optimal point can be obtained by reducing the difference between primal and dual problem cost functions, called the primal-dual gap.

$$\sum_i \big(|L_i U| - \chi_i L_i U\big) \tag{2.24}$$

Thus, in feasible region, solution in PDIPM framework can be obtained by solving the following set of equations.

$$\begin{aligned} &|\chi_i| \leq 1, \\ &\big(|L_i U| - \chi_i L_i U\big), \qquad i = 1, 2, \dots \\ &\mathbf{S}^T(H_{in}^0 - H_{in}^m + \mathbf{S}\Delta U) + \beta \mathbf{L} U \end{aligned} \tag{2.25}$$

However, absolute value in primal-dual gap is not differentiable. In order to achieve differentiability, $|L_iU|$ is approximated as $\sqrt{|L_iU|^2+\alpha}$. Which is differentiable and as $\alpha \to 0$, $\sqrt{|L_iU|^2+\alpha} \to |L_iU|$. Therefore, using small α values, differentiability will be achieved without deviating much from $|L_iU|$. Then using the Gauss Newton method, linear system of equations for ΔU and $\Delta\chi$ is obtained as follows.

$$\begin{bmatrix} \mathbf{S}^T\mathbf{S} & \beta\mathbf{L}^T \\ \mathbf{KL} & -\mathbf{E} \end{bmatrix} \begin{bmatrix} \Delta U \\ \Delta\chi \end{bmatrix} = - \begin{bmatrix} \mathbf{S}^T(H_{in}^0 - H_{in}^m) + \beta\mathbf{L}^T\chi \\ \mathbf{L}U - \mathbf{E}\chi \end{bmatrix}$$
$$\eta_i = \sqrt{(L_iU)^2+\alpha},\ \mathbf{E} = diag(\eta) \tag{2.26}$$
$$K_i = diag(1 - \frac{\chi_i L_i U}{\eta_i}),\quad i = 1, 2, \dots$$

At each iteration, individual updates for electrical properties and dual variables can be calculated from Equation 2.27, using Equation 2.26.

$$\Delta U = -\big(\mathbf{S}^T\mathbf{S} + \beta\mathbf{L}^T\mathbf{E}^{-1}\mathbf{KL}\big)^{-1}\big(\mathbf{S}^T(H_{in}^0 - H_{in}^m) + \beta\mathbf{L}^T\mathbf{E}^{-1}\mathbf{L}U\big)$$
$$\Delta\chi = -\chi + \mathbf{E}^{-1}\mathbf{L}U + \mathbf{EKL}\Delta U \tag{2.27}$$

For ensuring that dual variables, χ's, are in the feasible region for all indeces, $|\chi_i| < 1$, some form of normalization has to be applied for either the update itself or the updated dual variables.In the Iterative Fitting Approach applications, updated dual variables are normalized as follows at an iteration k.

$$\chi^k = \frac{\chi^{k-1} + \Delta\chi}{\max(\chi^{k-1} + \Delta\chi)} \tag{2.28}$$

2.1.5.4 Discretization of Total Variation Term

When $\mathbf{L}$ matrix in Equation 2.21 is generated using the derivative operator matrices constructed via central differencing formulas, ill-conditionedness of the problem decreases. However, ill-conditioned nature of the problem still prominent. Compared to Figure 2.2, in Figure 2.4 it can be seen that addition of Total Variation regularization with the $\mathbf{L}$ matrix constructed using central difference formulas reduces the ill-condition of the problem but compared to the Figure 2.3,

ill-condition of the problem is not reduced to a comparable level of Tikhonov regularization.

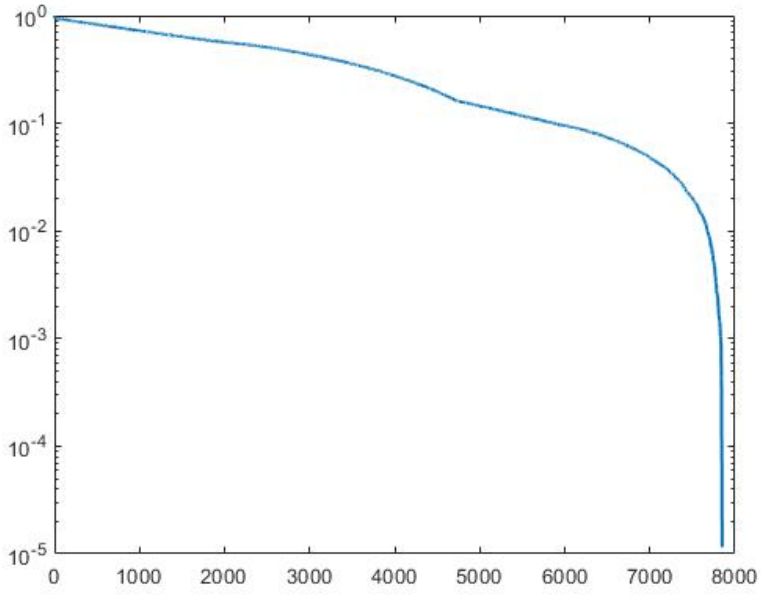

Figure 2.4: Normalized Singular Value Decomposition for Real and Imaginary Seperated **S** Matrix with Total Variation Regularization Using Central Difference Formulas

However, when forward or backward difference formulas are used ill-condition of the problem futher decreases, as it can be seen in Figure 2.5. Therefore, averaging of electrical property updates obtained via solution of Equation 2.20 using forward and backward differencing, is applied so that drawbacks of forward and backward difference formulas will be mitigated.

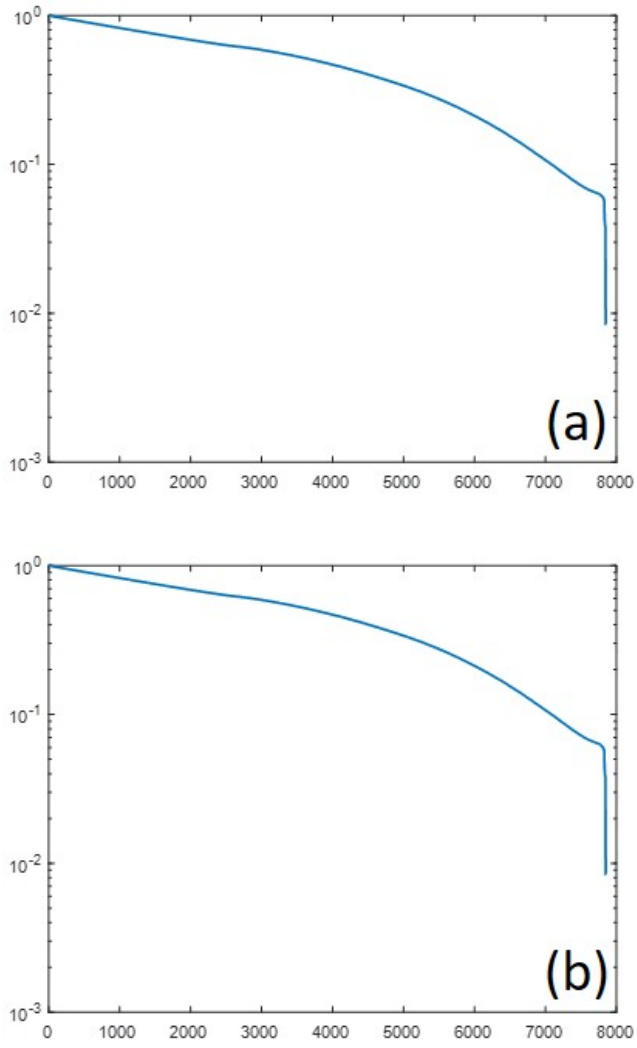

Figure 2.5: Normalized Singular Value Decomposition for Real and Imaginary Seperated **S** Matrix with Total Variation Regularization Using (a) Forward Difference Formulas (b) Backward Difference Formulas

2.1.6 Extension to 3D

From 2D central slice reconstructions of simulation and experimental phantoms(Figure 3.13(e,h) and 3.15(e,h) in Chapter 3), it can be seen that Iterative Fitting Approach results in inaccurate conductivity values for 3D objects. This problem arises since 2D forward problem formulation, Equation 2.3, results in inaccurate solution of H^+ in the slice. Therefore, electrical property updates cannot be obtained correctly which leads to inaccurate electrical property reconstructions.

For solving this problem, Iterative Fitting Approach is extended for obtaining 3D electrical property reconstructions so that solution of the 3D forward problem is similar to the measured H^+ and accurate conductivity values will be obtained using the Iterative Fitting Approach.

Another advantage of the 3D electrical property reconstruction is elimination of the z- independent electrical property assumption required for dimensionality reduction of the 3D formulations. This assumption is not valid for complex structures such as brain, where electrical properties vary in all 3 dimensions. With the 3D reconstruction method, electrical property reconstructions of 3D varying structures can be obtained more accurately.

However, for 3D reconstructions, required MRI scan time increases due to the fact that 3D H^+ data is required for the reconstruction. Moreover, required computation time and memory is also increased signifacntly due to the number of unknowns.

Determining the number of slices used for 3D Iterative Fitting Approach is critical since there will be error propagation from the boundary slices, top and bottom slices, which will effect the electrical property reconstructions. In Figure 2.6 (a-f), center slice of the conductivity reconstructions obtained via Iterative Fitting Approach with Tikhonov regularization at 5^{th} iteration using 5,7,9,11,13 and 15 slices are given respectively. It can be seen from the Figure 2.6 that using less than 9 slices results in erronous conductivity reconstructions. However, there

are no significant difference between conductivity reconstructions at the center slice when 11, 13 and 15 slices are used. Therefore, 11 slices will be used for the 3D Iterative Fitting Approach electrical property reconstructions for reducing the required computation time.

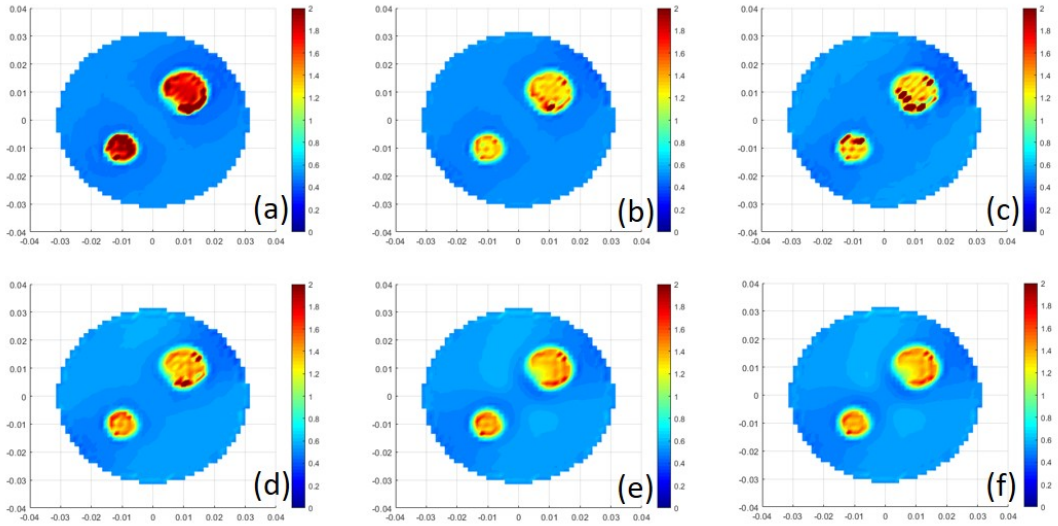

Figure 2.6: (a-f) Center Slice of the Conductivity Reconstruction obtained via Iterative Fitting Approach with Tikhonov Regularization using 5, 7, 9, 11, 13 and 15 Slices

2.2 Simulation Methods

Using the COMSOL Multiphysics, simulation phantoms are modeled and H^+ data for each phantom is generated. This generated H^+ data is used for electrical property reconstructions. Simulation phantoms are modeled based on the method proposed by Gurler [35].

First phantom modeled is the 2D simulation phantom, where infinitely long cylindrical object is assumed to be under the effect of the clockwise rotating radio-frequency (RF) field. Hence, 2D H^+ data that does not change in z- direction is obtained. With the assumption of infinitely long cylindrical object, it is also assumed that electrical properties does not change in z- direction. 2D triangular

mesh with 1 mm mesh size is used for the electromagnetic simulation of this phantom.

Second phantom modeled in the COMSOL Multiphysics, is a cylindrical object that is placed in a Quadrature Birdcage Coil (QBC). Using this phantom, 3D H^+ is generated. For enabling the use of H^+ in only the central slice of the object, electrical properties are given as z- independent. Such that assumption made for obtaining 2D equations will be somewhat satisfied. In Figure 2.7, model of this phantom is given.

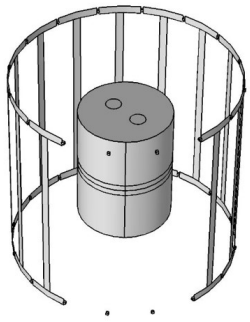

Figure 2.7: z- Indepedent 3D Phantom Model Inside the Quadrature Birdcage Coil (First 3 Rungs are not Shown)

Third phantom modeled is again a cylindrical object placed in a QBC, but electrical properties of the anomalies inside the phantom are z- dependent. In Figure 2.8, geometry of 3D varying anomalies inside this phantom along with the placement of this phantom inside the QBC is given. In this phantom, anomalies with different electrical properties are designed as 3 cylinders, height is 0.6 cm and radius is 1 cm, with centers in the center slice of the cylindrical object.

For 3D simulation phantoms, tetrahedron based, variable size mesh has been used for the phantom and the coil. The maximum element size was set to be 1.3 mm for the regions inside the phantom where $-0.5\ cm < z < 0.5\ cm$ and inside all of the capacitors, and 1 cm for the remaining parts of the phantom and for the dielectric regions of the coil.

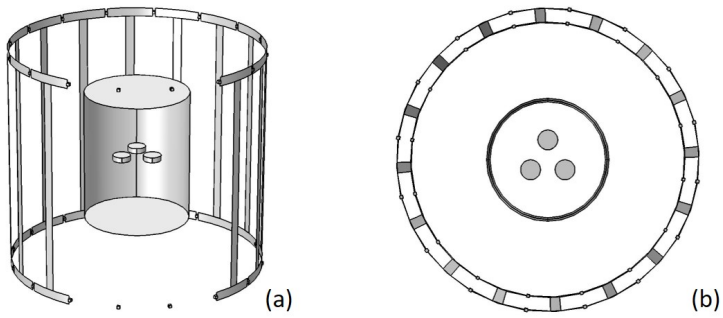

Figure 2.8: (a) 3D Phantom Model Inside the Quadrature Birdcage Coil (First 3 Rungs are not Shown) (b) xy- Cross Section of Anomalies at the Center Slice of 3D Phantom

2.3 Experimental Methods

2.3.0.1 Phantom Preparation

Experimental phantoms are designed as cylindrical z- independent phantoms with 15 cm height and 6 cm radius. Background of the phantom is an agar-saline gel (20 g/L $Agar$, 2 g/L $NaCl$, 1.5 g/L $CuSO_4$) with expected conductivity of 0.5 S/m [21]. Anomalies are created as cylindrical holes in the background agar-saline gel , with the same height as gel, filled with saline solution (6 g/L $NaCl$, 1.5 g/L $CuSO_4$). Anomalies have expected conductivity of 1 S/m [21].

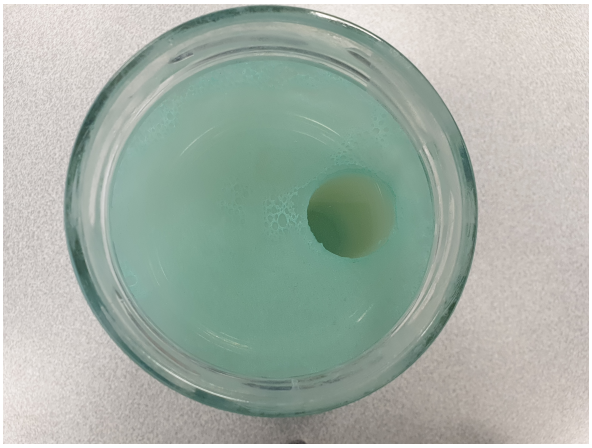

Figure 2.9: Top View of the Experimental Phantom used in 3D Reconstructions

2.3.0.2 Sequences and Parameters

For complex B_1^+ mapping, phase and magnitude maps of the B_1^+ obtained seperately using different pulse sequences. B_1^+ phase map is obtained via balanced Steady State Free Precision (bSSFP) pulse sequence. On the other hand, B_1^+ magnitude map is obtained using Bloch-Siegert Shift based method.

For the 2D reconstructions of the experimental phantoms, 2D bSSFP is used for the B_1^+ phase mapping at the central slice with the following sequence paramters: FOV = 20 $cm \times 20$ cm, Slice Thickness = 2 mm, Flip Angle = 40^o , TR/TE = 4.68/2.34 ms, Matrix Size= 128×128 and 1024 averages. 2D Bloch-Siegert Shift based method is used obtaining the B_1^+ magnitude, with the following sequence parameters: FOV = 20 $cm \times 20$ cm, Slice Thickness = 2 mm, Flip Angle = 55^o, TR = 100 ms, TE = 11 ms, Matrix Size= 128×128, 32 averages, Fermi pulse with off-resonance = 1000 Hz.

For the 3D reconstructions of the experimental phantoms, multi-slice bSSFP sequence is used for the B_1^+ phase mapping at the central slice with the following sequence paramaters: FOV = 17.5 $cm \times 17.5$ $cm \times 4$ cm, Slice Thickness = 2 mm, Flip Angle = 40^o , TR/TE = 4.58/2.29 ms, Matrix Size= $128 \times 128 \times 20$ and 32 averages. Multi-slice Bloch-Siegert Shift based method is used obtaining the B_1^+ magnitude, with the following sequence parameters: FOV = 17.5 $cm \times 17.5$ $cm \times$ 4 cm, Slice Thickness = 2 mm, Flip Angle = 55^o, TR = 100 ms, TE = 15 ms, Matrix Size= $128 \times 128 \times 20$, 16 averages, Fermi pulse with off-resonance = 1000 Hz and duration of 6 seconds.

In the B_1^+ phase data, linear phase shifts between slices are observed, due to the multi-slice acquisition. Phase shifts are shown in Figure 2.10(a) for the pixel at the center of the imaged object (b) for a pixel close to the edge of the imaged object. When a second order polynomial curve fit is used to determine the linear phase shifts for each pixel, it is observed that for each pixel slope of the linear phase shift is not identical therefore removal of the linear term in the second order polynomial for each pixel will not suffice. However, considering that imaged region in z- direction is relatively small, it can be assumed that phase

does not change significantly in z- direction. Therefore, phase is assumed to be constant in z- direction and phase of the center slice is assigned to the all the other slices.

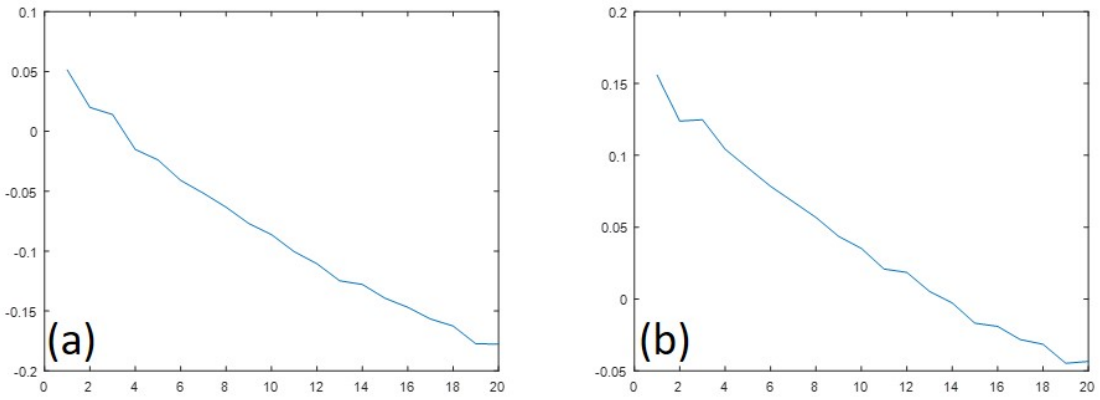

Figure 2.10: (a) Phase of the Center Pixel for All Slices (b) Phase of an Outer Pixel for All Slices

2.4 Selection of Initial Electrical Property Distributions

In Iterative Fitting Approach, initial electrical property distributions have to be assigned in order to solve the forward problem for the first iteration. For electrical property reconstructions of the simulation phantoms, initial electrical property distribution is selected as uniform electrical properties with the background electrical property values in the region of interest. For the experimental phantom, initial electrical properties distribution is selected as the uniform distribution of the expected electrical property values of the background in the region of interest. However, if the electrical property values are not known before hand, selection of the initial distribution can be done by selecting a uniform distribution of approximate average value of electrical properties in the region of interest.

Chapter 3

Results

3.1 Forward Problem Results

In order to test the solution of the forward problem, actual electrical properties of the simulation phantoms are for obtaining H^+ data for the simulation phantoms. H^+ data for the simulation phantoms are obtained using the COMSOL Multphysics and these H^+ data will be denoted as the measured H^+ data and H^+ obtained by solving the forward problem will be denoted as calculated H^+.

In Figure 3.1, (a) Magnitude of measured H^+ for 2D simulation phantom, (b) Magnitude of calculated H^+ for 2D simulation phantom and (c) difference between measured and calculated H^+ are given. From Figure 3.1, it can be seen that calculated H^+ matches the measured H^+ and difference between them is at most less than 1%. In fact this is only at the internal boundaries where we also expect numerical errors due to mesh based approximations. Since the internal boundaries are discontinuities in the electrical property distributions, difference between calculated and measured H^+ is more enhanced. Difference between calculated and measured H^+ is given in Figure 3.1(c). Figure 3.1 shows that using the forward problem H^+ can be solved accurately in 2D for the 2D simulation phantom.

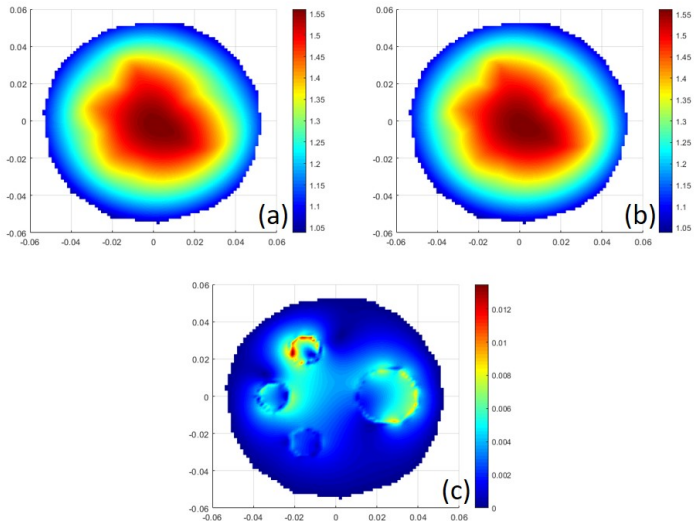

Figure 3.1: (a) Magnitude of Measured H^+ for 2D Simulation Phantom (b) Magnitude of Calculated H^+ for 2D Simulation Phantom (c) Magnitude of Difference Between Calculated and Measured H^+ for 2D Simulation Phantom

In Figure 3.2, (a) Magnitude of measured H^+ at the center slice for z- independent 3D simulation phantom, (b) Magnitude of calculated H^+ at the center slice for z- independent 3D simulation phantom and (c) difference between measured and calculated H^+ at the center slice are given. From Figure 3.2, it can be seen that difference between calculated H^+ and measured H^+ is around 10 % which incidicates that solution of the forward problem is erroneous for the single slice of 3D objects.

When 3D forward problem formulation is used for the 3D calculation of the H^+ in z- independent 3D simulation phantom, difference between measured and calculated H^+ reduces. In 3D case, 1^{st} and 21^{th} slices of the measured H^+ is also given as boundary conditions. In Figure 3.3, (a,c) first and (b,d) 11^{th} slices of magnitude of the measured and calculated H^+ are given. For the solution of the forward problem 21 slices are used. In Figure 3.4 (a-g), magnitude of the difference between measured and calculated H^+ at slices 1, 4, 7, 11, 15, 18 and 21 are given. Similar to the z- independent 3D simulation phantom case, difference between measured and calculated H^+ increases at the middle slices and decreases at the slices near the boundary layers.

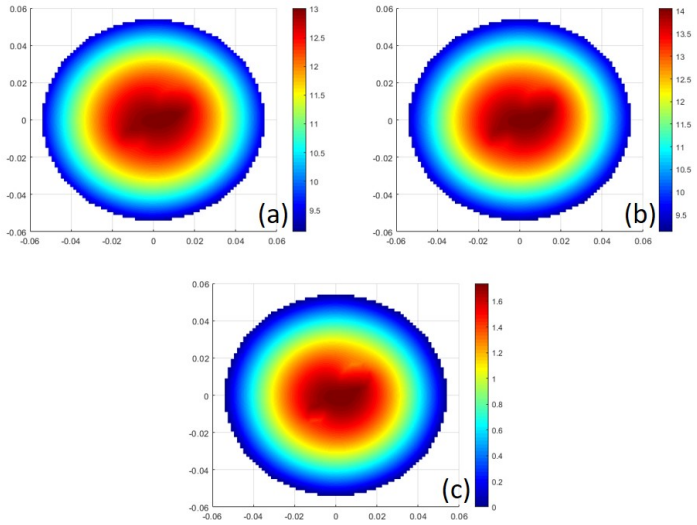

Figure 3.2: (a) Magnitude of Measured H^+ for z- Independent 3D Simulation Phantom at the Center Slice (b) Magnitude of Calculated H^+ for z- Independent 3D Simulation Phantom at the Center Slice (c) Magnitude of Difference Between Calculated and Measured H^+ for z- Independent 3D Simulation Phantom at the Center Slice

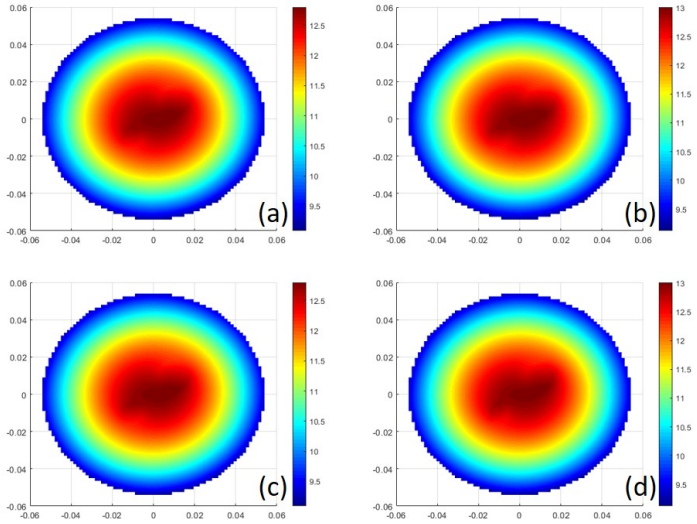

Figure 3.3: (a) Magnitude of Measured H^+ for z- Independent 3D Simulation Phantom at 1^{st} Slice (b) Magnitude of Measured H^+ for z- Independent 3D Simulation Phantom at 11^{th} Slice (c) Magnitude of Calculated H^+ for z- Independent 3D Simulation Phantom at 1^{st} Slice (d) Magnitude of Calculated H^+ for z- Independent 3D Simulation Phantom at 11^{th} Slice

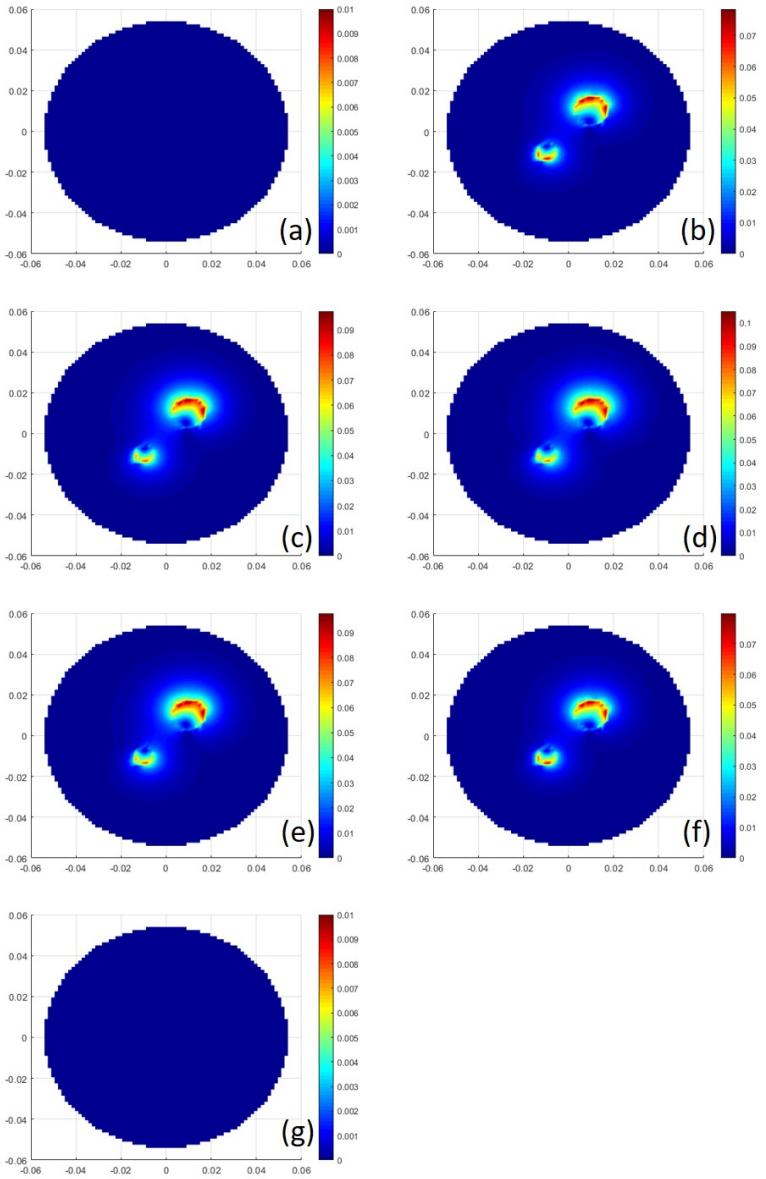

Figure 3.4: (a-g) Magnitude of the Difference Between Measured and Calculated H^+ for z- Independent 3D Simulation Phantom at Slices 1, 4, 7, 11, 15, 18 and 21

Figures 3.3 and 3.4 shows that using the 3D forward problem formulation, H^+ can be accurately calculated in 3D for 3D phantoms on the contrary to the forward problem solution for 3D phantom only at the central slice. In all slices, difference between measured and calculated H^+ is less than 1% but difference between them is even smaller near the boundary slices compared to the central slices. For example, difference at slice 18 and 4 is similar but they are less than the difference at the 11^{th} slice.

For the 3D simulation phantom case, where electrical properties vary in all directions, difference between calculated H^+ (using the 3D forward problem formulation) and öeasured H^+ is also less than 1% for all slices. For the solution of the forward problem in 21 slices, 1^{st} and 21^{th} slices chosen as boundary layers and value of the measured H^+ at these slices are used as boundary values. In Figure 3.5 (a-g), magnitude of the difference between measured and calculated H^+ at slices 1, 4, 7, 11, 15, 18 and 21 are given.

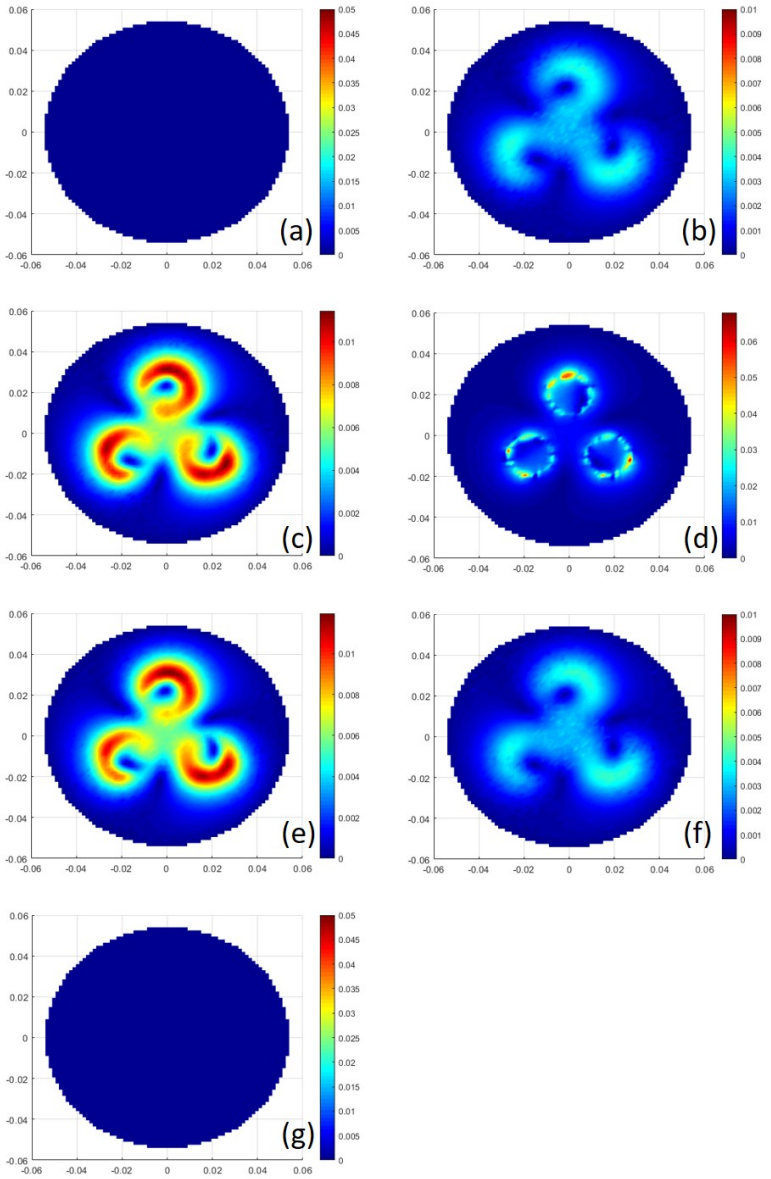

Figure 3.5: (a-g) Magnitude of the Difference Between Measured and Calculated H^+ for z- Independent 3D Simulation Phantom at Slices 1, 4, 7, 11, 15, 18 and 21

3.2 Electrical Property Reconstructions of 2D Objects

In Figure 3.6(a) actual conductivity distribution of the 2D phantom is given. Conductivity reconstruction obtained via std-MREPT and cr-MREPT are given in Figure 3.6(b) and (c) respectively. It can be seen that conductivity reconstruction obtained via std-MREPT method suffers from boundary artifacts and conductivity reconstruction obtained via cr-MREPT has the LCF artifact in the central region (highlighted with red circle).

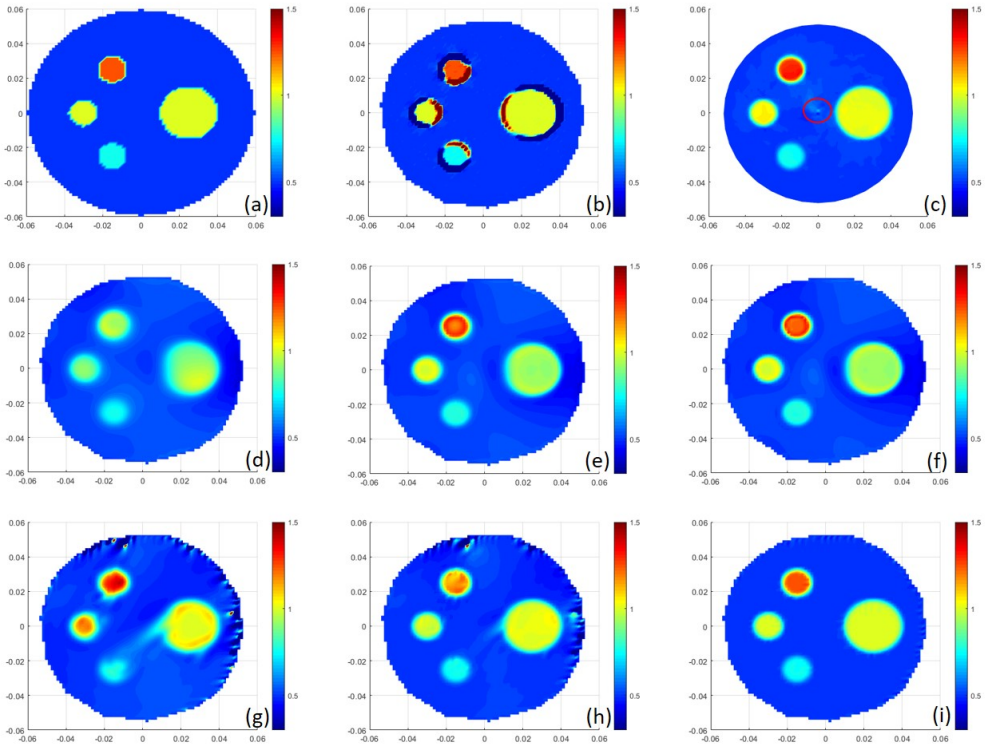

Figure 3.6: (a) Actual Conductivity Distribution of the 2D Phantom (b) std-MREPT Conductivity Reconstruction of the 2D Phantom (c) cr-MREPT Conductivity Reconstruction of the 2D Phantom (d-f) 1^{st}, 3^{rd} and 5^{th} Iteration of the Conductivity Reconstruction via Iterative Fitting Approach with Tikhonov Regularization, $\lambda = 10^{-3}$ (g-i) 2^{nd}, 4^{th} and 7^{th} Iteration of the Conductivity Reconstruction via Iterative Fitting Approach with Total Variation Regularization, $\beta = 10^{-8}$

Figure 3.6(d-f) shows the 1^{st}, 3^{rd} and 5^{th} iteration of the conductivity reconstruction via Iterative Fitting Approach with Tikhonov regularization with regularization parameter λ chosen as 10^{-3}. As it can be from the 5^{th} iteration of Iterative Fitting Approach with Tikhonov Regularization, obtained conductivity reconstruction is free of both boundary and LCF artifact.

Similarly, Figure 3.6(g-i) shows the 2^{nd}, 4^{th} and 7^{th} iteration of the conductivity reconstruction via Iterative Fitting Approach with Total Variation regularization with regularization parameter β chosen as 10^{-8}. As it can be from the Figure 3.6(i), obtained conductivity reconstruction is, again, free of both boundary and LCF artifact. However, compared to the conductivity reconstructions obtained using Total variation regularization has smoother values inside the tissues whereas ones obtained using Tikhonov regularization slightly varies inside the tissues.

In Figure 3.7 and 3.8, conductivity profiles of conductivity reconstructions obtained via Iterative Fitting Approach with Tikhonov regularization using regularization parameters $\lambda = 10^{-2},\ 5 \times 10^{-3},\ 10^{-3},\ 5 \times 10^{-4},\ 10^{-4}$ derivative of these proflies are given respectively.

In Figure 3.9 and 3.10, conductivity profiles of conductivity reconstructions obtained via Iterative Fitting Approach with Total Variation using regularization parameters $\beta = 10^{-7},\ 5 \times 10^{-8},\ 10^{-8},\ 5 \times 10^{-9},\ 10^{-9}$ derivative of these profiles are given respectively.

For the 2D simulation phantom, Figures 3.7 and 3.9 indicate that for Tikhonov regularization as λ increases transition between tissues become smoother and when λ decreases transitions become sharper but conductivity values vary inside the tissues where it should be constant. For Total Variation regularization,β value is chosen as 10^{-7}, transition between tissues become overly smoothened but for lower values of β transition between tissues are sharper and close to each other. However, when β value is chosen as 10^{-9}, conductivity values inside the tissues varies where conductivity values are expected to be constant.

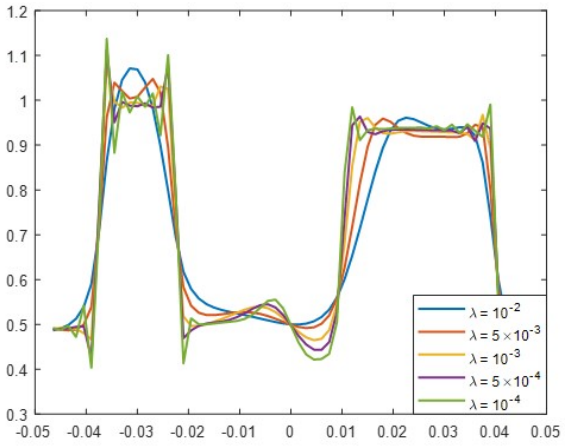

Figure 3.7: Profiles of the Conductivity Reconstructions obtained via Iterative Fitting Approach with Tikhonov Regularization Using Different λ Values on x-axis

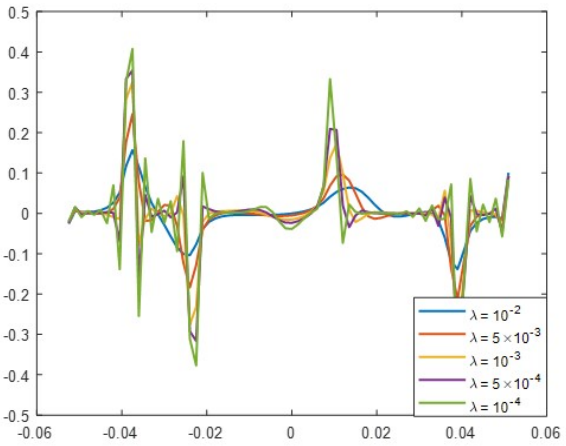

Figure 3.8: Derivatives of the Profiles in Figure 3.7

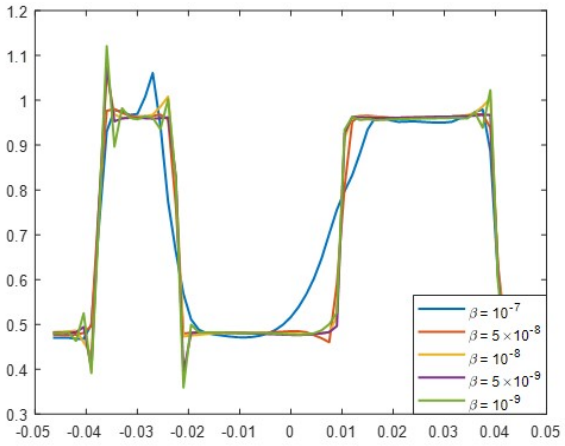

Figure 3.9: Profiles of the Conductivity Reconstructions obtained via Iterative Fitting Approach with Total Variation Regularization Using Different β Values on x- axis

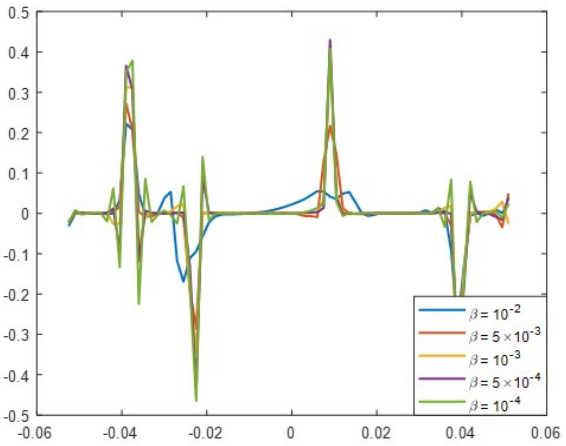

Figure 3.10: Derivatives of the Profiles in Figure 3.9

Using the derivatives of the profiles given in Figures 3.7 and 3.9, Full Width Half Maximum (FWHM) of the reconstructions can be obtained as a resolution measure.FWHM values are obtained as in Table 3.1, for both regularizations on a uniform grid with pixel size of 1.5 mm.

Tikhonov Regularization		
λ	FWHM (mm)	FWHM (pixels)
10^{-2}	5.1	$3-4$
5×10^{-3}	3.5	$3-4$
10^{-3}	2.5	$1-2$
5×10^{-4}	2.1	$1-2$
10^{-4}	2	$1-2$
Total Variation Regularization		
β	FWHM (mm)	FWHM (pixels)
10^{-7}	6.3	$4-5$
5×10^{-8}	2.3	$1-2$
10^{-8}	2.1	$1-2$
5×10^{-9}	2.1	$1-2$
10^{-9}	1.8	$1-2$

Table 3.1: FWHM Values Obtained for Iterative Fitting Approach with Tikhonov and Total Variation Regularization

From Table 3.1, it can be seen that reconstructions obtained using Tikhonov regularization can match the FWHM of the reconstructions obtained using Total Variation regularization as β decreases. Compared to the Tikhonov regularization, conductivity reconstruction obtained using Total Variation regularization results in more smooth conductivity values inside the tissues. However, for both regularization as λ and β values decrease variance in the conductivity values increases especially at tissue transitions resulting in inaccurate conductivity values.

3.3 2D Electrical Property Reconstructions of z- Independent 3D Objects

For 2D reconstruction of 3D z- independent objects, H^+ data only at the central slice is used. In iterative Fitting Approach reconstructions, 2D forward problem is solved for obtaining the H^+ data of the center slice of the 3D z-independent object at each iteration. Uniform grid with pixel size of 1.5 mm is used for the electrical property reconstructions obtained via Iterative Fitting Approach. For the noisy simulation cases, SNR is chosen as 350.

In Figure 3.11, conductivity reconstructions for the z- independent 3D simulation phantom via cr-MREPT method is shown. (a) cr-MREPT conductivity reconstruction without regularization (b) cr-MREPT conductivity reconstruction with artificial diffusion (c) cr-MREPT conductivity reconstruction with Tikhonov regularization (addition of $||u||_2^2$ term to the cost function) (d) cr-MREPT conductivity reconstruction with L_2 norm of gradient of unknowns (addition of $||\nabla u||_2^2$ term to the cost function) (e) cr-MREPT conductivity reconstruction with Tikhonov regularization (addition of $||\nabla^2 u||_2^2$ term to the cost function). In Figure 3.12, conductivity reconstructions obtained with the same methods in Figure 3.11 is given when the noise is present in the H^+ data.

In Figure 3.13, (a) std-MREPT conductivity reconstruction of the z- independent 3D simulation phantom, (b) cr-MREPT conductivity reconstruction of the z- independent 3D simulation phantom, (c-e) 1^{st}, 5^{th} and 9^{th} iteration of the conductivity reconstruction via iterative fitting approach with Tikhonov regularization with regularization parameter $\lambda = 5 \times 10^{-2}$ and (f-h) 3^{rd}, 9^{th} and 13^{th} iteration of the conductivity reconstruction via iterative fitting approach with Total Variation regularization with regularization parameter $\beta = 10^{-6}$ (i) profiles of the conductivity reconstructions obtained via Iterative Fitting Approach using Tikhonov and Total Variation regularizations (j) derivatives of the profiles in (i), are given. In Figure 3.14, 1^{st}, 5^{th} and 9^{th} iteration of the conductivity reconstruction via Iterative Fitting Approach with Tikhonov (a-c) and Total Variation (d-f) regularizations of z- independent 3D simulation phantom with noise is shown.

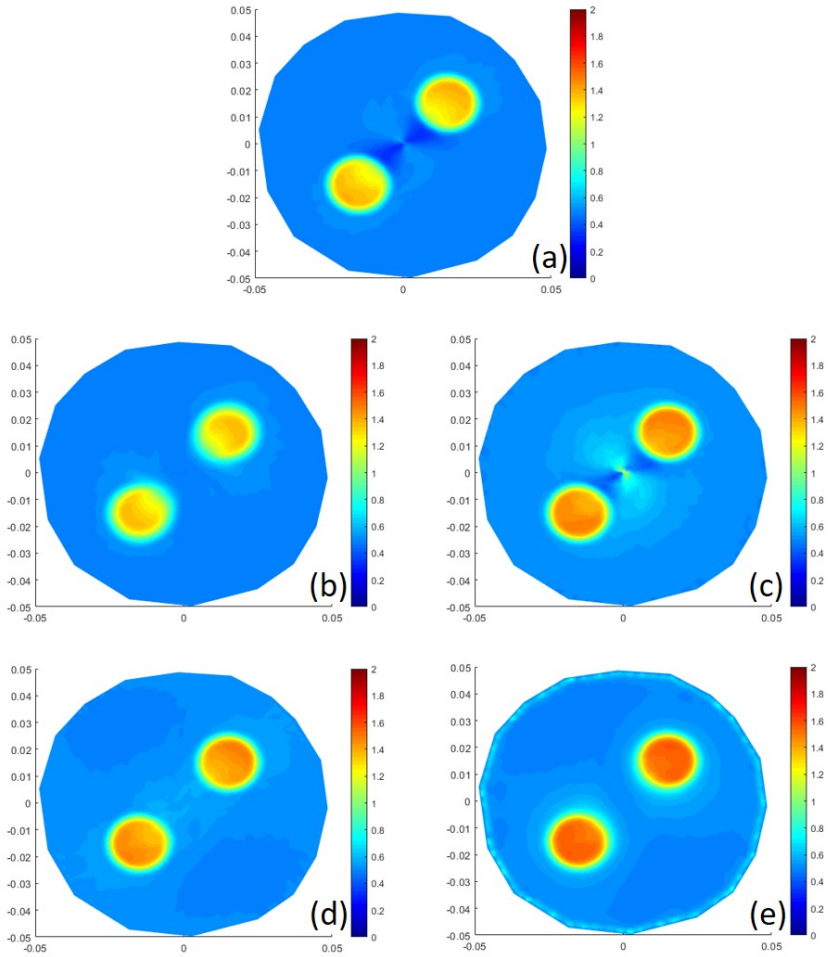

Figure 3.11: (a) cr-MREPT Conductivity Reconstruction of z- independent 3D Simulation Phantom (b) cr-MREPT Conductivity Reconstruction of z- independent 3D Simulation Phantom with Artificial Diffusion (c $= -10^{-1}$(c) cr-MREPT Conductivity Reconstruction with the Addition of Tikhonov Regularization ($\lambda = 10^7$) of z- independent 3D Simulation Phantom (d) cr-MREPT Conductivity Reconstruction with the Addition of L_2 Norm of Gradient of Unknowns ($\lambda = 5 \times 10^2$) of z- independent 3D Simulation Phantom (e) cr-MREPT Conductivity Reconstruction with the Addition of Laplacian Regularization ($\lambda = 10^{-2}$) of z- independent 3D Simulation Phantom

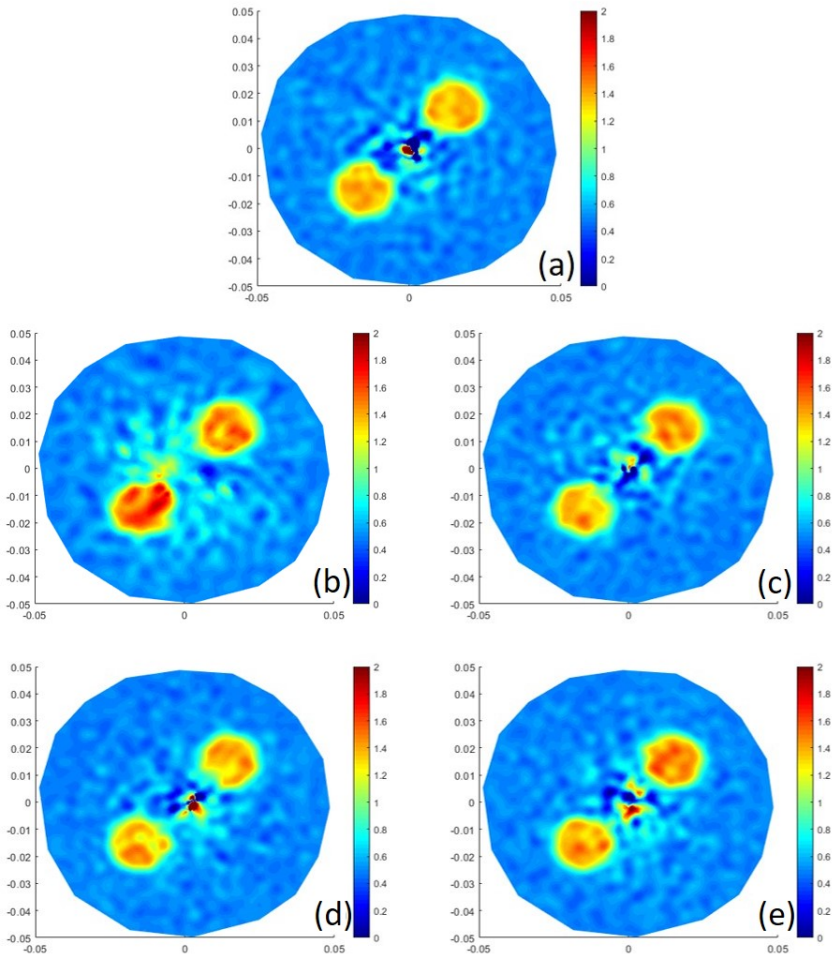

Figure 3.12: (a) cr-MREPT Conductivity Reconstruction of z- independent 3D Simulation Phantom with Noise (b) cr-MREPT Conductivity Reconstruction of z- independent 3D Simulation Phantom with Artificial Diffusion ($c = -10^{-1}$) with Noise (c) cr-MREPT Conductivity Reconstruction with the Addition of Tikhonov Regularization $\lambda = 10^6$ of z- independent 3D Simulation Phantom with Noise (d) cr-MREPT Conductivity Reconstruction with the Addition of L_2 Norm of Gradient of Unknowns $\lambda = 5 \times 10^1$ of z- independent 3D Simulation Phantom with Noise (e) cr-MREPT Conductivity Reconstruction with the Addition of Laplacian Regularization $\lambda = 10^{-4}$ of z- independent 3D Simulation Phantom with Noise (SNR = 350)

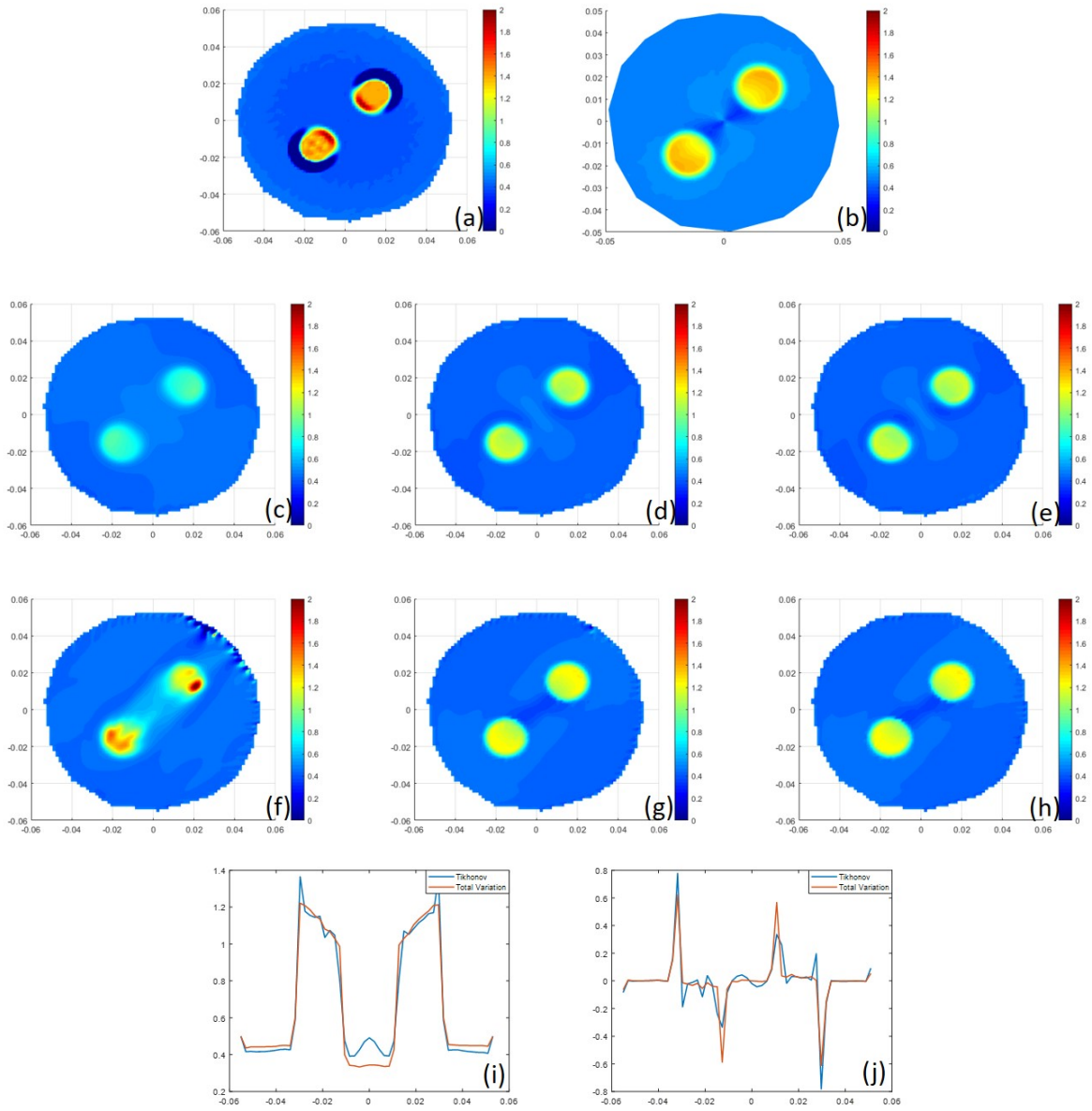

Figure 3.13: (a) std-MREPT Conductivity Reconstruction of the z- independent 3D Simulation Phantom (b) cr-MREPT Conductivity Reconstruction of the z- independent 3D Simulation Phantom (c-e) 1^{st}, 5^{th} and 9^{th} Iteration of the Conductivity Reconstruction via Iterative Fitting Approach with Tikhonov Regularization, $\lambda = 5 \times 10^{-2}$ (f-h) 3^{rd}, 9^{th} and 13^{th} Iteration of the Conductivity Reconstruction via Iterative Fitting Approach with Total Variation Regularization, $\beta = 10^{-6}$ (i) Profiles of the Conductivity Reconstructions Obtained via Iterative Fitting Approach using Tikhonov and Total Variation regularizations (j) Derivatives of the Profiles in (i)

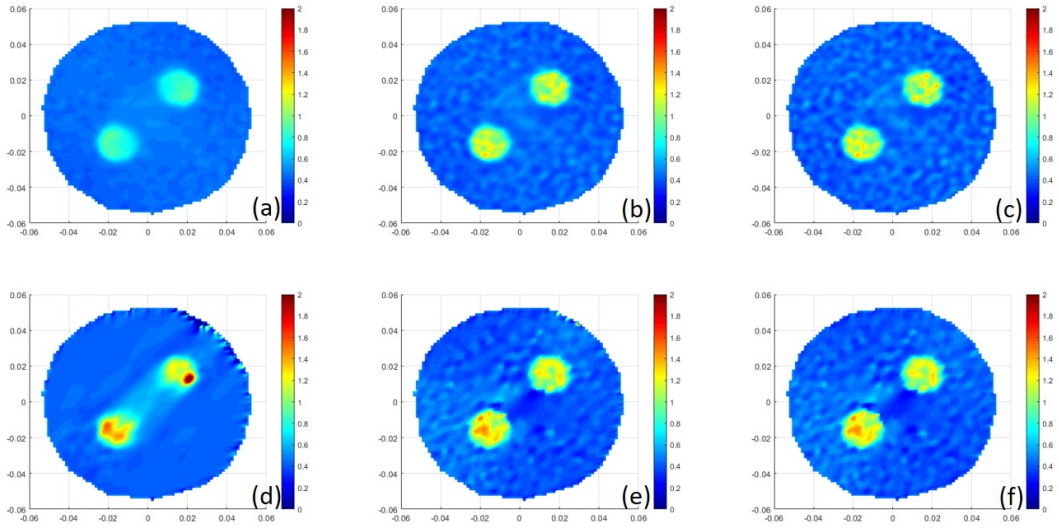

Figure 3.14: (a-c) 1st, 5th and 9th Iteration of the Conductivity Reconstruction via Iterative Fitting Approach with Tikhonov Regularization of z- independent 3D Simulation Phantom with Noise, $\lambda = 5 \times 10^{-2}$ (d-f) 3rd, 9th and 13th Iteration of the Conductivity Reconstruction via Iterative Fitting Approach with Total Variation Regularization, $\beta = 10^{-6}$ of z- independent 3D Simulation Phantom with Noise (SNR = 350)

Conductivity reconstructions obtained using Iterative Fitting Approach with Tikhonov regularization (Figure 3.13(c-e)) and with Total Variation regularization (Figure 3.13(f-h)) for the 3D z- independent simulation phantom, are free of boundary artifacts. However, effect of the LCF artifact can be seen in the conductivity reconstructions. While the anomalies and background are clearly separated in the conductivity reconstructions obtained via Iterative Fitting Approach, resulting conductivity values are inaccurate in the sense that conductivity values of the anomalies are 1.5 S/m and anomalies in the reconstructions have values around 1.2 S/m. Which is the result of the inaccurate solution of the 2D forward problem solution for 3D objects. While Total Variation regularization results in smoother conductivity values inside the tissue regions, compared to the Tikhonov regularization for 3D z- independent simulation phantom. When noise is present, reconstruction obtained are similar to each other meaning that smoothness advantage of the Total Variation is mitigated.

In Figure 3.15; (a) std-MREPT conductivity reconstruction of the experiment

phantom, (b) cr-MREPT conductivity reconstruction of the experiment phantom, (c-e) 1^{st}, 5^{th} and 9^{th} iteration of the conductivity reconstruction via iterative fitting approach with Tikhonov regularization with regularization parameter $\lambda = 10^{-2}$ and (f-h) 3^{rd}, 11^{th} and 16^{th} iteration of the conductivity reconstruction via iterative fitting approach with Total Variation regularization with regularization parameter $\beta = 10^{-6}$ (i) profiles of the conductivity reconstructions obtained via Iterative Fitting Approach using Tikhonov and Total Variation regularizations (j) derivatives of the profiles in (i), are given. are given.

Similar to the z- independent 3D simulation phantom conductivity reconstructions using the Iterative Fitting Approach, conductivity reconstruction of the experimental phantom obtained using the Iterative Fitting Approach, Figure 3.15, is free of boundary and LCF artifacts but conductivity values at the anomalies are low compared to the std-MREPT and cr-MREPT reconstructions obtained using the same H^+ data.

From Figure 3.13(e,h) and 3.15(e,h), it can be seen that for both simulation and experimental phantoms, regardless of the choice of the regularization (Tikhonov or Total Variation), Iterative Fitting Approach results in low conductivity values at the anomalies which is the result of the inaccurate solution of 2D forward problem for 3D center slice H^+ data.

Despite the inaccurate conductivity values, profiles of the conductivity reconstructions for both simulation and experimental phantoms and their derivatives show that FWHM of the conductivity reconstructions are 2-3 mm. Since the electrical property reconstructions are obtained using 1.5 mm uniform grid, FWHM is around 2 pixels for used λ and β for Tikhonov and Total Variation regularizations.

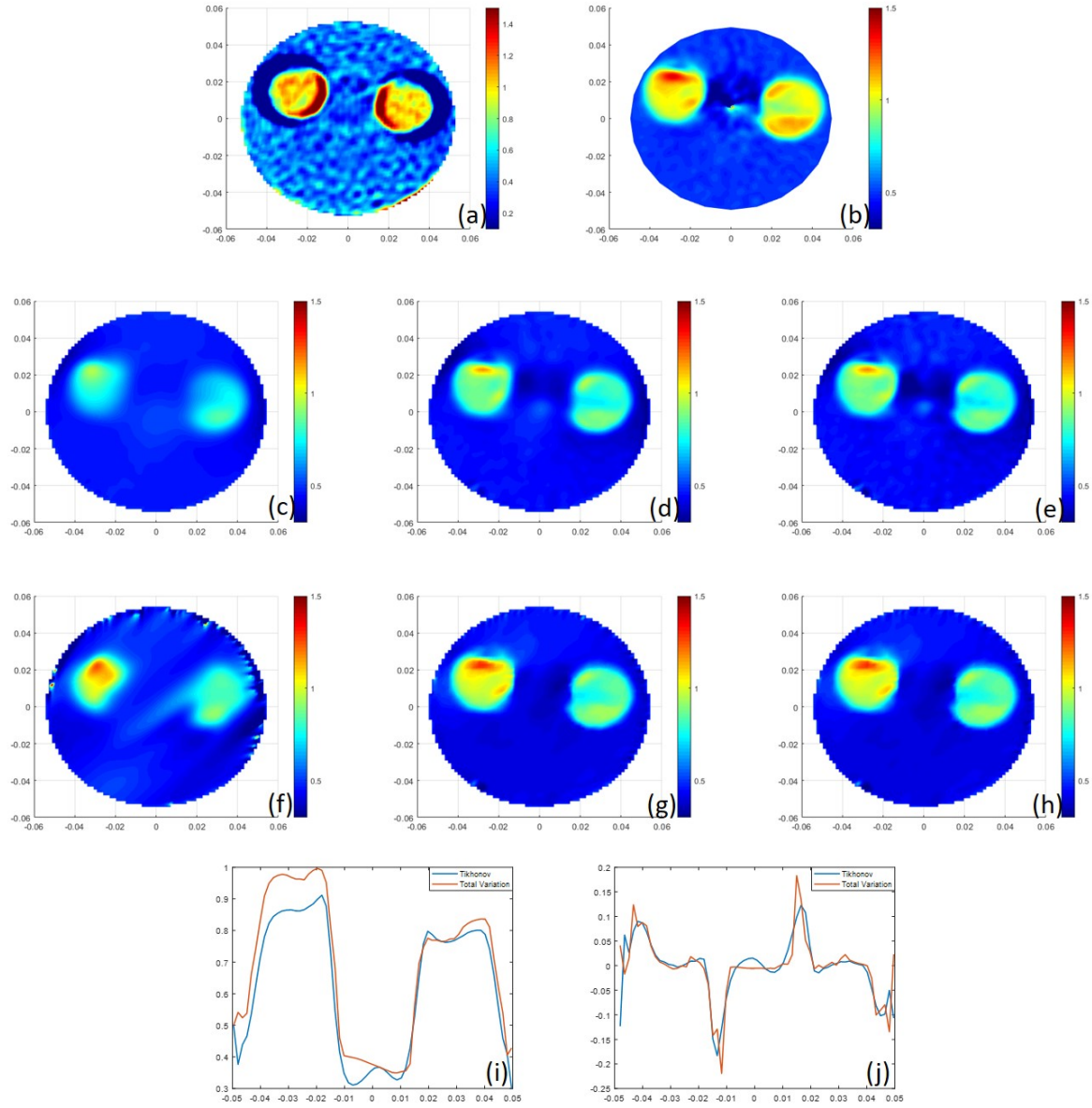

Figure 3.15: (a) std-MREPT Conductivity Reconstruction of Experiment Phantom (b) cr-MREPT Conductivity Reconstruction of Experiment Phantom (c-e) 1^{st}, 5^{th} and 9^{th} Iteration of the Conductivity Reconstruction via Iterative Fitting Approach with Tikhonov Regularization, $\lambda = 10^{-2}$ (f-h) 3^{rd}, 11^{th} and 16^{th} Iteration of the Conductivity Reconstruction via Iterative Fitting Approach with Total Variation Regularization, $\beta = 10^{-6}$ (i) Profiles of the Conductivity Reconstructions Obtained via Iterative Fitting Approach using Tikhonov and Total Variation regularizations (j) Derivatives of the Profiles in (i)

3.4 3D Electrical Property Reconstructions of z- Independent 3D Objects

For the 3D electrical property reconstruction of z- independent 3D objects using Iterative Fitting Approach, 11 slices are used and voxel size is chosen as 1.5 mm for z-independent 3D simulation phantom and 2 mm for the experimental phantom. 6^{th} slice is chosen as the center slice and 5 slice offset is used. First and last 3 slices of conductivity reconstructions are not shown due to the error propagation from boundary layers. This error occurs because electrical properties at the boundary layers are assumed to be uniform where, it is not uniform for z-independent anomalies

In Figure 3.16, (a-f) 4^{th} to 8^{th} slices of 11 slice 3D cr-MREPT reconstruction for the z- independent 3D simulation phantom, (g) conductivity profile on Line 1(Figure 3.16 (f)) and (h) conductivity profile on Line 2(Figure 3.16 (f)) are given. As it can be seen from the Figure 3.16 (a-f), LCF artifact occurs at each slice of the 3D cr-MREPT reconstruction.

In Figure 3.17, (a-f) 4^{th} to 8^{th} slices of 11 slice Iterative Fitting Approach with Tikhonov regularization ($\lambda = 10^{-2}$) conductivity reconstruction obtained at the 5^{th} iteration for the z- independent 3D simulation phantom, (g) conductivity profile on Line 1 (Figure 3.17 (f)) and (h) conductivity profile on Line 2 (Figure 3.17 (f)) are given.

In Figure 3.18, (a-f) 4^{th} to 8^{th} slices of 11 slice Iterative Fitting Approach with Total Variation regularization ($\beta = 10^{-6}$) conductivity reconstruction obtained at the 9^{th} iteration for the z- independent 3D simulation phantom, (g)conductivity profile on Line 1 (Figure 3.18 (f)) and (h) conductivity profile on Line 2 (Figure 3.18 (f)) are given.

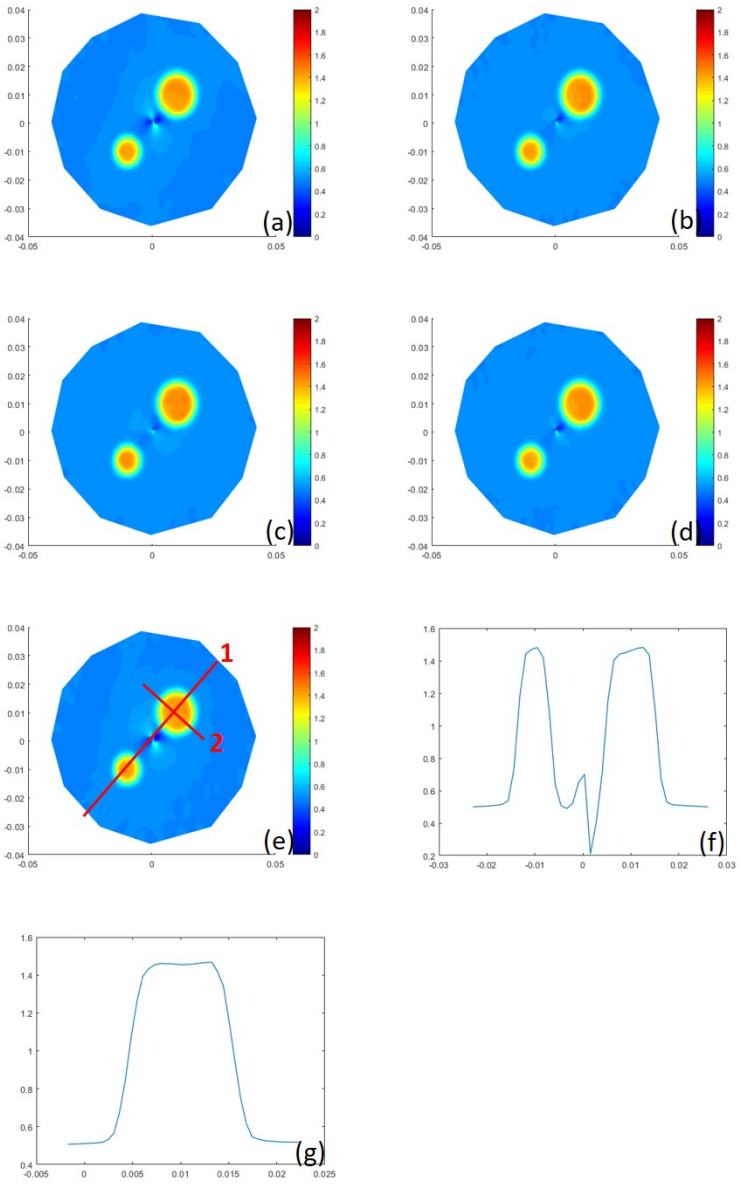

Figure 3.16: (a-e) 4^{th} to 8^{th} Slices of 11 Slice 3D cr-MREPT Reconstruction for the z- Independent 3D Phantom (f) Profile on Line 1 (g) Profile on Line 2 (First and last 3 Slices are not Shown)

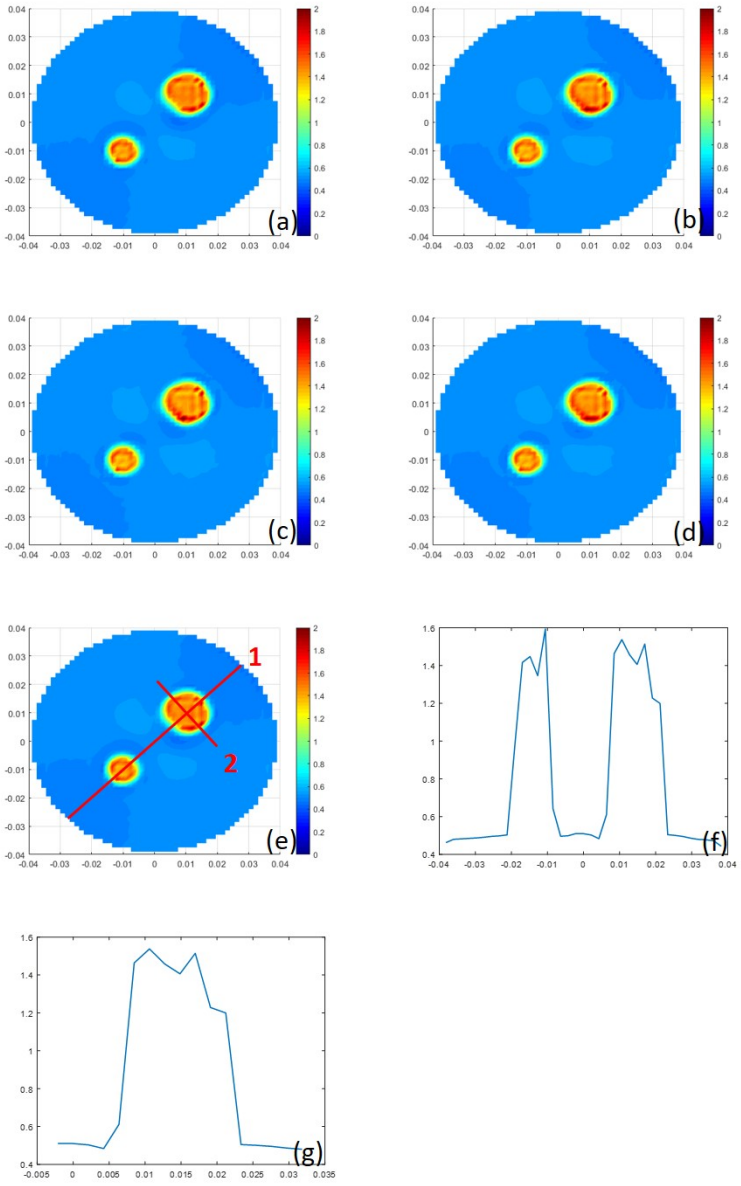

Figure 3.17: (a-e) 4^{th} to 8^{th} Slices of 11 Slice Iterative Fitting Approach with Tikhonov Regularization ($\lambda = 10^{-2}$) Conductivity Reconstruction at Iteration 5 for the z- independent 3D Simulation Phantom (f) Profile on Line 1 and (g) Profile on Line 2

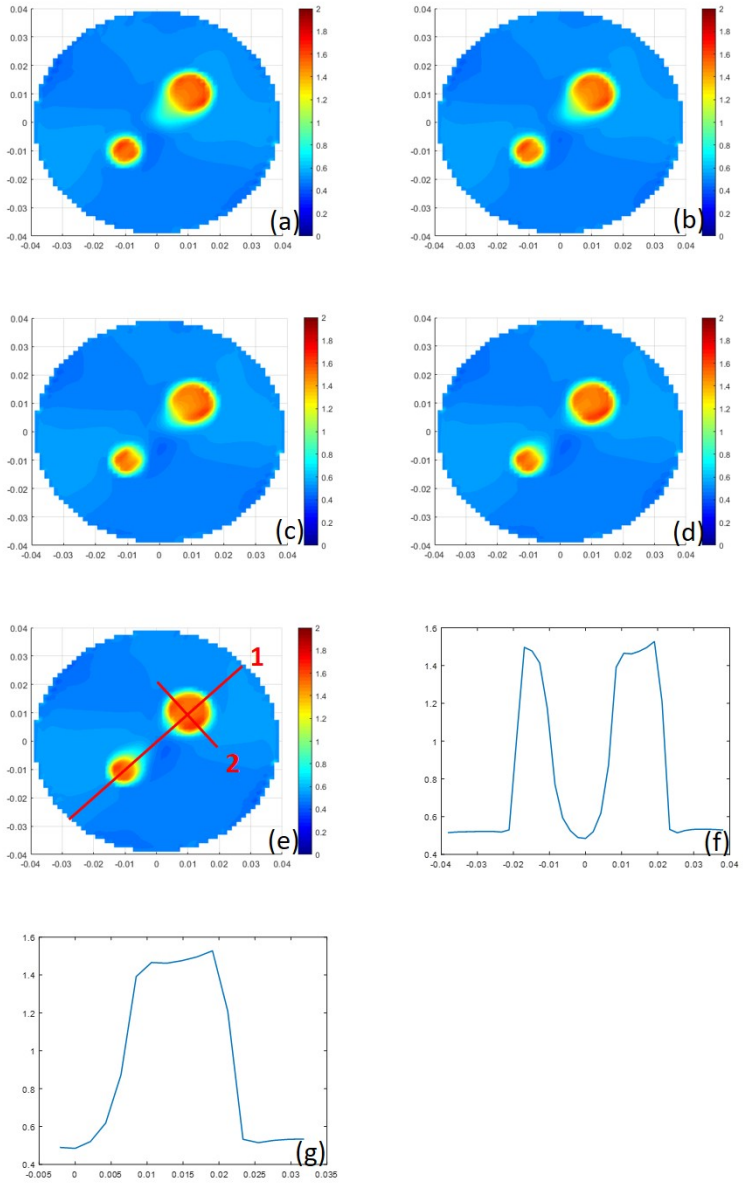

Figure 3.18: (a-e) 4^{th} to 8^{th} Slices of 11 Slice Iterative Fitting Approach with Total Variation Regularization ($\beta = 10^{-6}$) Conductivity Reconstruction at Iteration 9 for the z- independent 3D Simulation Phantom (f) Profile on Line 1 and (g) Profile on Line 2

From Figures 3.16, 3.17 and 3.18, it can be seen that when Iterative Fitting Approach with Tikhonov or Total Variation regularization is used for 3D electrical property reconstruction of the z- independent 3D simulation phantom is used, LCF artifact is eliminated. However, on the contrary to expected, conductivity reconstructions obtained using Total Variation regularization does not result in sharper transitions between tissue boundaries compared to the Tikhonov regularization. From the profiles, Figure 3.17(g) and Figure 3.18(g), it can be seen that LCF artifact is eliminated for both cases but tissue transitions are similar. However, inside the tissues, Total Variation regularization results in smoother conductivity values compared to the Tikhonov regularization. Which is advantageous since inside the tissues conductivity values are constant.

For 3D electrical property reconstruction of z- independent experimental phantom, 11 slices are used. 6^{th} slice is chosen as the center slice and 5 slice offset is used. First and last 3 slices of conductivity reconstructions are not shown due to the error propagation from boundary layers similar to the z- independent 3D phantom case.

When 3D Iterative Fitting Approach is used for the experimental phantom, similar results are obtained to z- independent 3D phantom. However, due to the presence of the noise, resulting conductivity reconstructions are also noisy.

In Figure 3.19, (a-e) 4^{th} to 8^{th} slices of 11 slice 3D cr-MREPT reconstruction for the experimental phantom is given. As it can be seen from the Figure 3.19 (a-f), LCF artifact occurs at each slice of the 3D cr-MREPT reconstruction.

In Figure 3.20, (a-e) 4^{th} to 8^{th} slices of 11 slice Iterative Fitting Approach with Tikhonov regularization ($\lambda = 0.1$) conductivity reconstructions obtained at the 9^{th} iteration for the z- independent 3D simulation phantom is given.

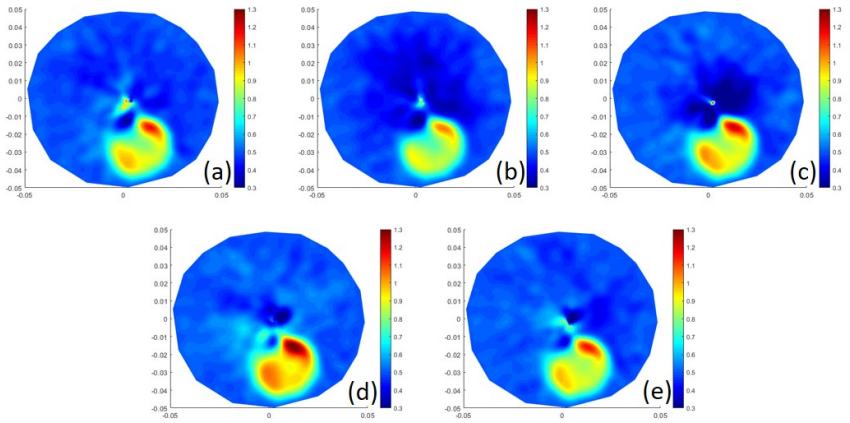

Figure 3.19: (a-e) 4^{th} to 8^{th} Slices of 11 Slice 3D cr-MREPT Reconstruction for the Experimental Phantom

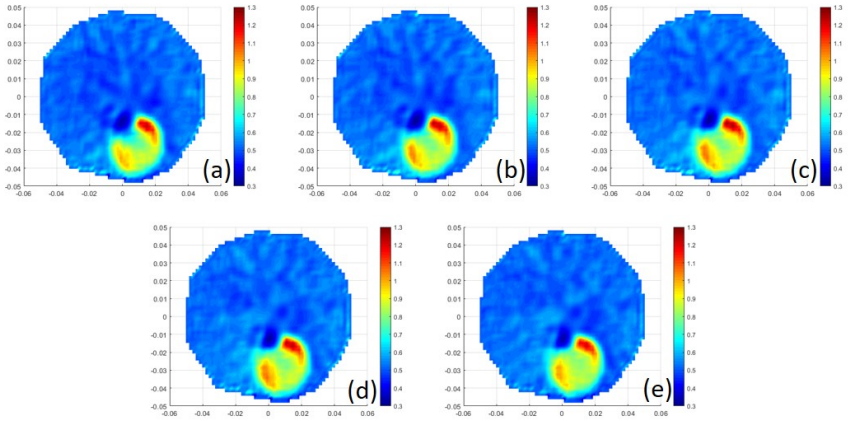

Figure 3.20: (a-e) 4^{th} to 8^{th} Slices of 11 Slice Iterative Fitting Approach with Tikhonov Regularization ($\lambda = 10^{-1}$) Conductivity Reconstruction at Iteration 9 for the Experimental Phantom

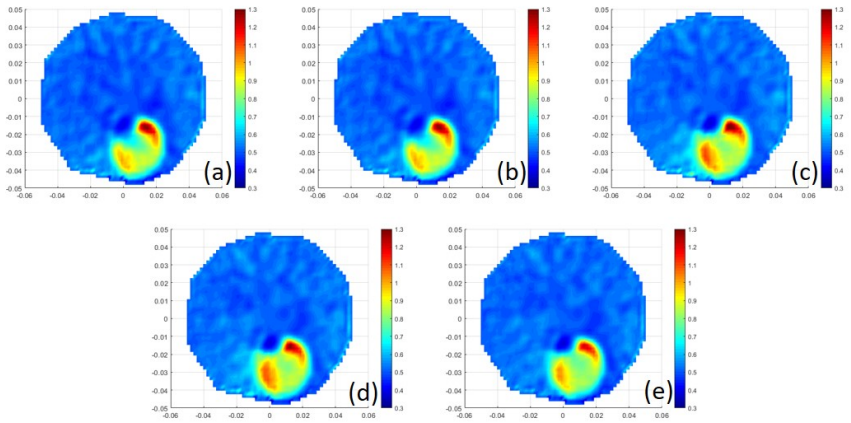

Figure 3.21: (a-e) 4^{th} to 8^{th} Slices of 11 Slice Iterative Fitting Approach with Total Variation Regularization ($\beta = 10^{-4}$) Conductivity Reconstruction at Iteration 12 for the Experimental Phantom

From Figures 3.20 and 3.21, it can be seen that conductivity reconstructions obtained via 3D Iterative Fitting Approach using Tikhonov and Total Variation regularization does not have LCF artifacts. For the experimental phantom, reconstructions obtained via Tikhonov and Total Variation regularizations result similar tissue transitions.

3.5 3D Electrical Property Reconstructions of 3D Objects

For the 3D electrical property reconstruction of 3D simulation phantom using Iterative Fitting Approach, 11 slices are used and voxel size is chosen as 1.5 mm for 3D simulation phantom . 6^{th} slice is chosen as the center slice and 5 slice offset is used. For the 3D simulation phantom case, first and last slice have the exact electrical property values as the boundary layers therefore there is no error propagation from boundary layers. Hence, all 11 slices can be accurately reconstructed.

In Figure 3.22, (a-k) 1^{st} to 11^{th} slices of 11 slice 3D cr-MREPT reconstruction for the z- ,dependent 3D simulation phantom, (l) x- profile of the conductivity

for the top anomaly at the 6^{th} slice and (m) y- profile of the conductivity for the top anomaly at the 6^{th} slice (n) z- profile of the conductivity for the top anomaly are given.

In Figure 3.23, (a-k) 1^{st} to 11^{th} slices of Iterative Fitting Approach with Tikhonov regularization ($\lambda = 10^{-2}$) conductivity reconstruction obtained at the 3^{rd} iteration for the 3D simulation phantom, (l) x- profile of the conductivity for the top anomaly at the 6^{th} slice and (m) y- profile of the conductivity for the top anomaly at the 6^{th} slice (n) z- profile of the conductivity for the top anomaly are given.

In Figure 3.24, (a-k) 1^{st} to 11^{th} slices of Iterative Fitting Approach with Tikhonov regularization ($\beta = 10^{-6}$) conductivity reconstruction obtained at the 5^{th} iteration for the 3D simulation phantom, (l) x- profile of the conductivity for the top anomaly at the 6^{th} slice and (m) y- profile of the conductivity for the top anomaly at the 6^{th} slice (n) z- profile of the conductivity for the top anomaly are given.

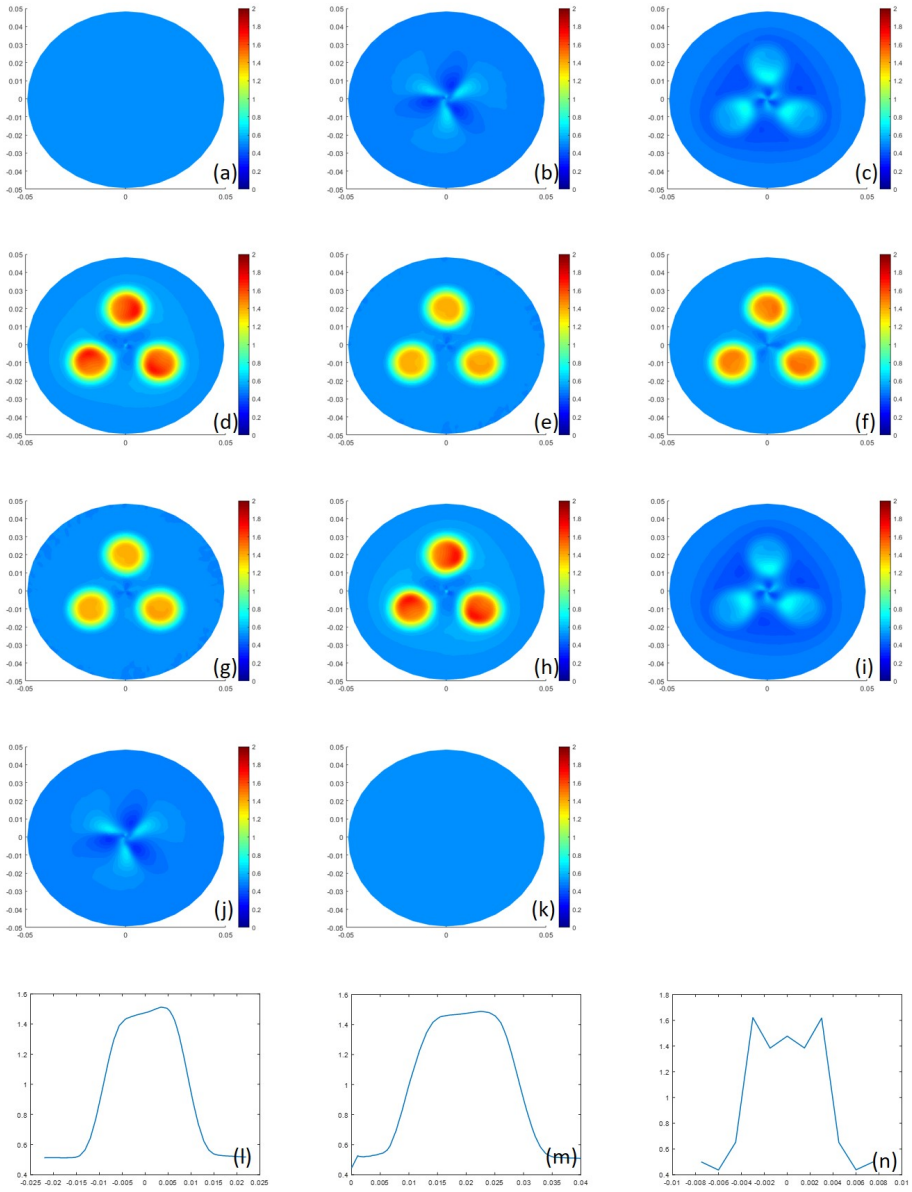

Figure 3.22: (a-k) 1st to 11th Slices of 11 slice 3D cr-MREPT Reconstruction for the z- Independent 3D Simulation Phantom, (l) x- Profile of the Conductivity for the Top Anomaly at the 6th Slice (m) y- Profile of the Conductivity for the Top Anomaly at the 6th Slice (n) z- Profile of the Conductivity for the Top Anomaly

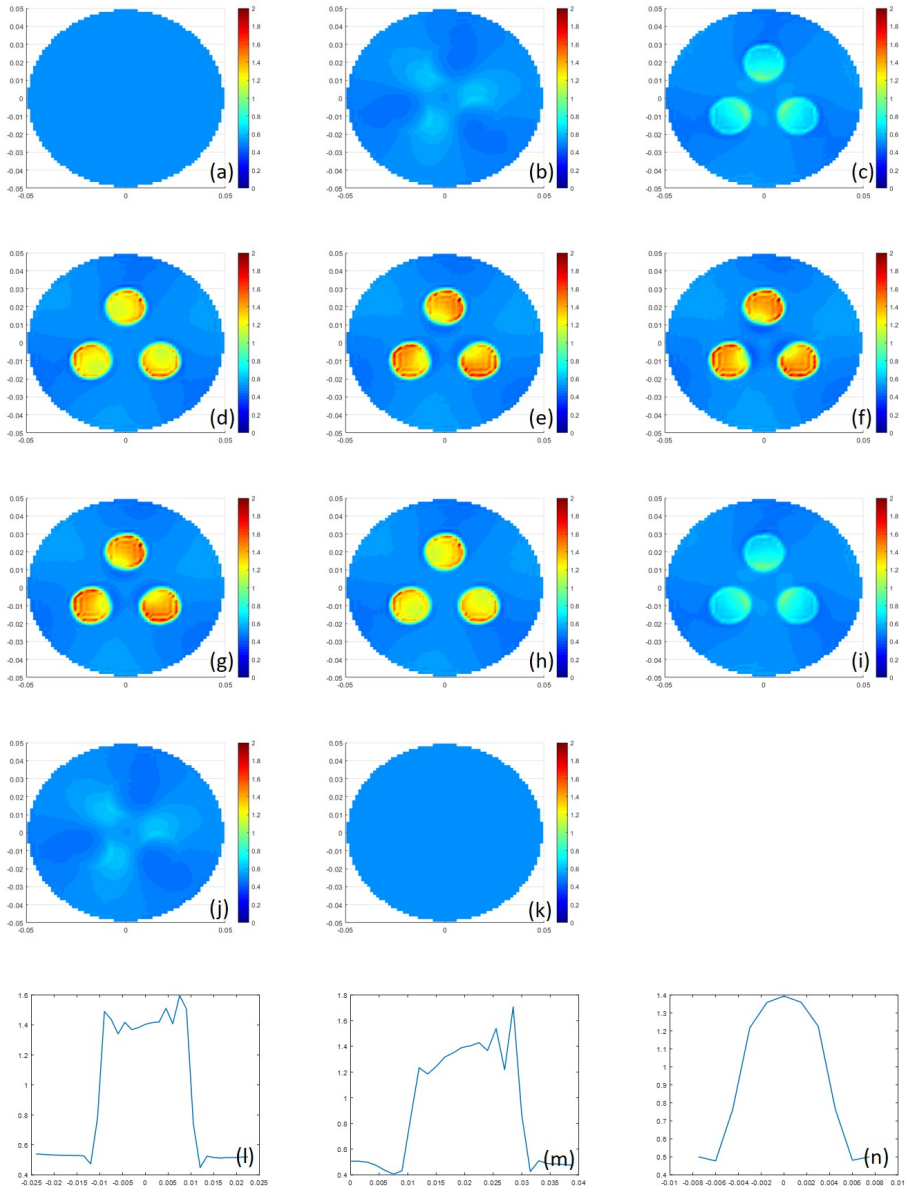

Figure 3.23: (a-k) 1^{th} to 11^{th} Slices of Iterative Fitting Approach with Tikhonov Regularization ($\lambda = 10^{-2}$) Conductivity Reconstruction Obtained at the 3^{rd} Iteration for the 3D Simulation Phantom, (l) x- Profile of the Conductivity for the Top Anomaly at the 6^{th} Slice (m) y- Profile of the Conductivity for the Top Anomaly at the 6^{th} Slice (n) z- Profile of the Conductivity for the Top Anomaly

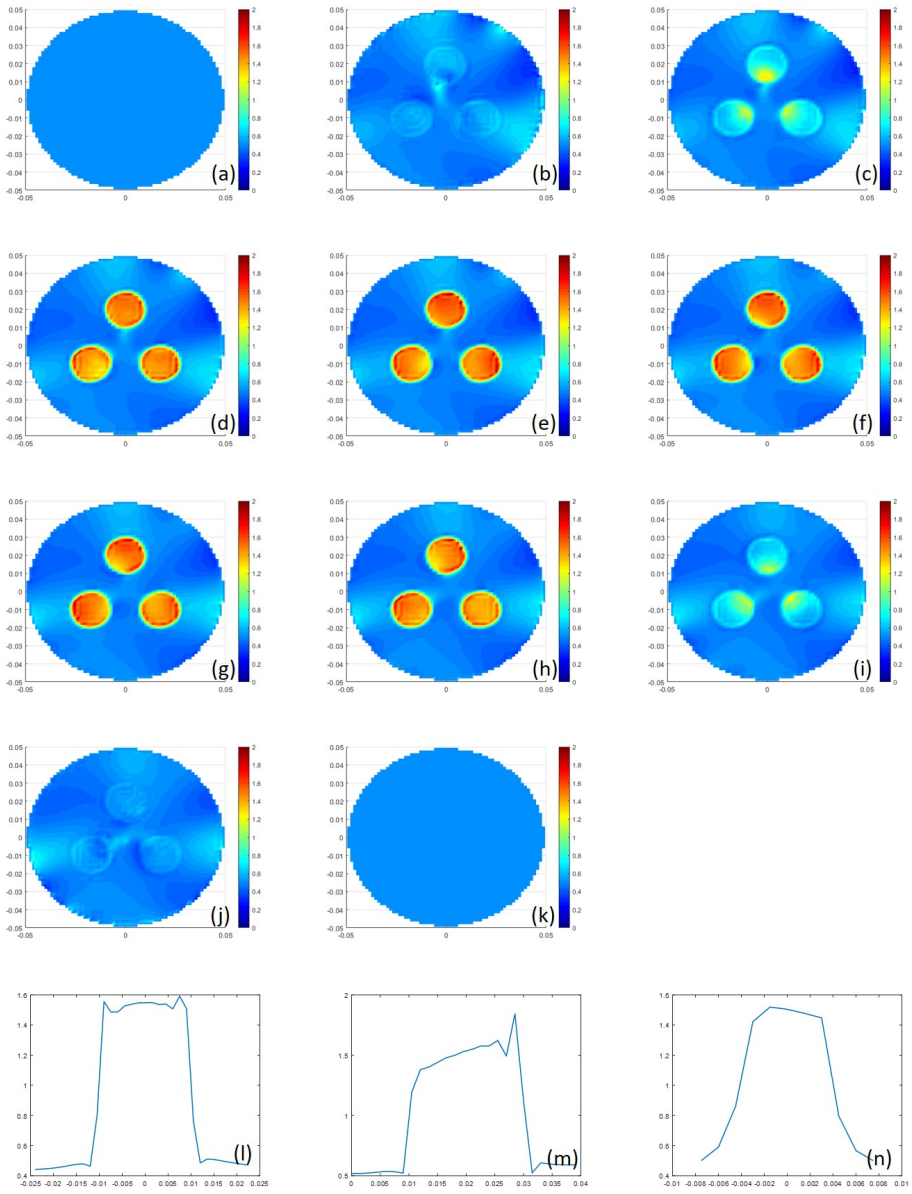

Figure 3.24: (a-k) 1^{th} to 11^{th} Slices of Iterative Fitting Approach with Total Variation Regularization ($\beta = 10^{-6}$) Conductivity Reconstruction Obtained at the 5^{th} Iteration for the 3D Simulation Phantom, (l) x- Profile of the Conductivity for the Top Anomaly at the 6^{th} Slice (m) y- Profile of the Conductivity for the Top Anomaly at the 6^{th} Slice

From Figures 3.17 and 3.18, it can be seen that when Iterative Fitting Approach with Tikhonov or Total Variation regularization is used for 3D electrical property reconstruction of the 3D simulation phantom is used, conductivity changes in all directions are captured. Similar to the previous results, conductivity reconstructions obtained using Total Variation regularization are smoother inside the tissues compared to the conductivity reconstructions obtained via Tikhonov regularization. No significant difference between conductivity reconstructions obtained via Tikhonov and Total Variation regularizations, can be observed at the tissue transitions. From the profiles given in Figure 3.17(l,m,n) and 3.18(l,m,n), it can be seen that transitions between low and high conductivity regions are similar for both regularizations.

Chapter 4

Conclusion and Discussion

MREPT carries a potential for being an important diagnostic tool in medicine, since contrast between benign and malign tissues can be obtained via noninvasive procedure without the need for external hardwares. Widely used std-MREPT method causes electrical property reconstructions with boundary artifacts between tissue transitions due to "Local Homogeneity Assumption" and obtained electrical property reconstructions are significantly affected from noise. Which detriments std-MREPT's potential for the clinical applications. On the other hand, cr-MREPT method eliminates the boundary artifact problem of the std-MREPT and it is less susceptible to noise. However, cr-MREPT method suffers from the LCF artifact, which occurs at the positions where magnitude of the convective field is low. In this thesis, Iterative Fitting Approach is developed for cr-MREPT, which aims to obtain electrical property reconstructions without boundary and LCF artifacts.

In the development of Iterative Fitting Approach, first forward problem of obtaining H^+ using the electrical properties is formulated using the cr-MREPT equation. Forward problem is discretized using central differencing formulas so that solution of the forward problem can be obtained via the Finite Difference Method. Using the uniqueness theorem proved by Ammari, solution of the forward problem is obtained in the desired ROI inside the imaged object. Then,

forward problem is solved using the electrical properties from previous iteration to obtain calculated H^+ for that iteration. In order to obtain a solution for the electrical properties inside the ROI, norm of the difference between measured H^+ and calculated H^+ is minimized. By Taylor series expansion and ignoring higher order terms, calculated H^+ is formulated in terms of calculated H^+ at that iteration, Jacobian matrix and the electrical property updates for that iteration. By solving this minimization problem, electrical property updates that minimizes the difference is obtained for each iteration. However, real and imaginary parts of the unknowns are seperated in the solution process. Final electrical property reconstructions are obtained after the sufficient number of iterations.

Obtaining electrical properties from the difference between measured and calculated H^+ is a ill-conditioned problem. Therefore, in order to obtain solution for electrical property updates at each iteration regularization is used. Tikhonov and Total Variation regularization is used to reduce the ill-conditionedness of the problem. When Tikhonov regularization is used, minimization problem is still quadratic and solution for the electrical property updates can be obtained with ease. When Total Variation regularization is used, due to the fact that L_1 norm is not differentiable, solution can only be obtained via approximations. Primal Dual Interior Point Method is used for the realization of the Total Variation regularization.

When 2D Iterative Fitting Approach with Tikhonov and Total Variation regularization is used for 2D simulation phantom in noiseless environment, obtained conductivity values are accurate and LCF artifact is eliminated in the reconstructions. Using the profiles on the x- axis of the conductivity reconstructions obtained using Iterative Fitting Approach with Tikhonov and Total Variation regularization with different regularization parameters, spatial resolution properties of the developed method is analyzed. By taking the derivative of these profiles, FWHM of the conductivity reconstructions is calculated. Calculated FWHM values indicate that depedending on the regularization reconstructions obtained with both Tikhonov and Total Variation regularization can have FWHM value of 1-2 pixels. Which shows that using Iterative Fitting Approach, high resolution electrical property reconstructions can be obained regardless of the choice

of the regularization. However, reconstructions obtained using Total Variation regularization has smoother conductivity values inside the tissue regions.

When 2D Iterative Fitting Approach with Tikhonov and Total Variation regularization is used for 3D z- independent object, obtained conductivity reconstructions are free of boundary and LCF artifacts but conductivity values are inaccurate (conductivity of 1.5 S/m for anomalies and 0.5 S/m for background, reconstructed conductivity of 1.2 S/m for anomalies and 0.4 S/m for background). The reason behind this is the inaccurate solution of the 2D forward problem for the center slice of the 3D z- independent simulation phantom. In the noisy environment, Iterative Fitting Approach still manages to eliminate the LCF artifact but there is no clear difference between electrical property reconstructions obtained via Tikhonov and Total Variation regularization. This shows that in a noisy environment, smoothness advantage of the Total Variation regularization disappears. Reconstructions obtained for the center slice of the z-independent experimental phantom also shows that conductivity values are inaccurate (expected conductivity of 1 S/m for anomalies and 0.5 S/m for background, reconstructed conductivity of 0.8 S/m for anomalies and 0.4 S/m for background). Despite the inaccurate conductivity values, resulting conductivity reconstructions are free of LCF artifact. Falling in line with the noisy simulation case, reconstruction obtained using Tikhonov and Total Variation regularization do not have clear difference between them.

Iterative Fitting Approach is extended for 3D electrical property reconstruction such that forward problem is solved in 3D and electrical property reconstructions are also obtained in 3D. Conductivity reconstructions obtained via 3D Iterative Fitting Approach, has the accurate conductivity values (conductivity of 1.5 S/m for anomalies and 0.5 S/m for background, reconstructed conductivity of 1.5 S/m for anomalies and 0.5 S/m for background) and free of boundary and LCF artifacts. Another benefit of the 3D reconstruction is that complex structures with electrical properties that varies in all directions can be imaged without any assumption of z- indepencency. Iterative Fitting Approach with Total Variation regularization results in smoother conductivity values inside the tissues, compared to the Tikhonov regularization. When 3D Iterative Fitting Approach is used

for z- independent experimental pahntom, this advantage fades because of the presence of the noise, therefore similar reconstructions for both Tikhonov and Total Variation regularizations are obtained.

3D Iterative Fitting Approach with Tikhonov or Total Variation regularization yields accurate, high resolution and artifact free conductivity reconstructions. Even though, Total Variation regularization results in smoother conductivity values inside the tissues, this advantage disappers with the presence of the noise. Moreover, on the contrary to the literature, Tikhonov and Total Variation regularizations have similar transitions across tissue boundaries in electrical property reconstructions obtained via Iterative Fitting Approach. Since smoothness advantage of the disappears in a noisy environment and spatial resolutions of the reconstruction obtained via Iterative Fİtting Approach with Tikhonov and Total Variation regularization are similar, Tikhonov regularization is more favorable to use in real life applications.

In the electrical property reconstructions obtained 3D Iterative Fitting Approach, first and last 3 slice are erronous due to the error propagation from the boundary layers. Which indicates that only 5 slices of a 11 slice reconstruction is usable. For solving this issue, implementation of the Iterative Fitting Approach without boundary nodes can be developed. Moreover, 3D Iterative Fitting Approach requires high computation time and memory for electrical property reconstructions due to the increased number of unknowns. As a future work, solution of the linear systems at each iteration can be obtained via iterative methods that requires less memory and that are parallelizable. Such that memory requirement can be reduced by using iterative methods instead of direct methods and computation time can be reduced by the parallel implementation of the iterative methods for solution of linear systems. Even if the memory and computational time requirements are reduced using iterative solvers and parallelization techniques, in order to reconstruct elelcrical properties in large region Iterative Fitting Approach should be used in a high performance setup. Again, as a future work Iterative Fitting Approach can be implemented in a high performance computing setup so that electrical property reconstructions in large region of interest can be obtained.

Bibliography

[1] A. J. Surowiec, S. S. Stuchly, J. R. Barr, and A. Swarup, "Dielectric Properties of Breast Carcinoma and the Surrounding Tissues," *IEEE Transactions on Biomedical Engineering*, vol. 35, no. 4, pp. 257-263, 1988.

[2] C. L. R. J. W. Joines, Y. Zhang, C. Li, and R. Jirtle, "The measured electrical properties of normal and malignant human tissues from 50 to 900 MHz," *Med Phys.*, vol. 21, no. 4, pp. 547-550, 1994.

[3] U. Katscher, T. Voigt, C. Findeklee, P. Vernickel, K. Nehrke, and O. Dossel, "Determination of electric conductivity and local sar via b1 mapping," *IEEE Transactions on Medical Imaging*, vol. 28, no. 9, p. 1365-1374, 2009.

[4] G. S. E Balidemaj, H Kok, and G. Schooneveldt"Hyperthermia treatment planning for cervical cancer patients based on electrical conductivity tissue properties acquired in vivo with EPT at 3 T MRI," *International Journal of Hyperthermia*, vol. 32, pp. 558-568, 2016.

[5] P. F. F Salinas, J Lancaster, and P. Fox, "3D modeling of the total electric field induced by transcranial magnetic stimulation using the boundary element method," *Physics in Medicine and Biology*, vol. 54, pp. 3631-3647, 2009.

[6] D. C. Barber and B. H. Brown, "Applied potential tomography," *Journal of Physics E: Scientic Instruments*, vol. 17, p. 723, 1984.

[7] A. Mcewan, G. Cusick, and D. S. Holder, "A review of errors in multi-frequency eit instrumentation," *Physiological Measurement*, vol. 28, no. 7, 2007.

[8] H. Griffiths, "Magnetic induction tomography," *Measurement Science and Technology*, vol. 12, p. 1126, 2001.

[9] N. G. Gencer and M. N. Tek, "Electrical Cconductivity Iimaging via Ccontactless Measurements," *IEEE Transactions on Medical Imaging*, vol. 181, no. 17, p. 617-627, 1999.

[10] N. G. Gencer and M. N. Tek, "Forward problem solution for electrical conductivity imaging via contactless measurements," *Physics in Medicine and Biology*, vol. 44, p. 927-939, R. L. A. 1999.

[11] G. C. Scott, M. L. G. Joy, R. L.Ãrmstrong, and R. M. Henkelman, "Measurement of nonuniform current density by magnetic resonance," *IEEE Transactions on Medical Imaging*, vol. 10, pp. 362-374, 1991.

[12] Y. Z. Ider and O. Birgul, "Use of the magnetic field generated by the internal distribution of injected currents for electrical impedance E. J. W. tomography (MREIT)," *ELEKTRIK*, vol. 6, pp. 215-225, 1998.

[13] J. K. Seo, J.-R. Yoon, E. J. Woo, and O. Kwon, "Reconstruction of conductivity and current density images using only one component of magnetic field measurements," *IEEE Transactions on Biomedical Engineering*, vol. 50, pp. 1121-1124, 2003.

[14] Y. Z. Ider and S. Onart, "Algebraic reconstruction for 3D magnetic resonance electrical impedance tomography (MREIT) using one component of magnetic flux dEensJity," W. J*PhySeosiological Measurement*, vol. 25, p. 281, 2004.

[15] J. K. Seo, E. J. Woo, and O. Kwon, "Magnetic resonance electrical impedance tomography (MREIT): conductivity and current density imaging," *Journal of Physics: Conference Series*, vol. 12, p. 140, 2005.

[16] L. Özparlak and Y. Z. Ider, "Induced current magnetic resonance–electrical impedance tomography," *Physiological Measurement*, vol. 26, no. 2, 2005.

[17] E. M. Haacke, L. S. Petropoulos, E. W. Nilges, and D. H. Wu, "Extraction of conductivity and permittivity using magnetic resonance imaging," *Physics in Medicine and Biology*, vol. 36, p. 723-734, Jan 1991.

[18] H. Wen, "Noninvasive quantitative mapping of conductivity and dielectric distributions using rf wave propagation effects in high-field mri," *Medical Imaging 2003: Physics of Medical Imaging*, Sep 2003.

[19] J. Liu, Y. Wang, U. Katscher, and B. He, "Electrical properties tomography based on B_1 maps in MRI: Principles, applications, and challenges," *IEEE Transactions on Biomedical Engineering*, vol. 64, no. 11, p. 2515–2530, 2017.

[20] U. Katscher and C. A. V. D. Berg, "Electric properties tomography: Biochemical, physical and technical background, evaluation and clinical applications," *NMR in Biomedicine*, vol. 30, no. 8, 2017.

[21] F. S. H?afalir, O. F. Oran, N. Gurler, and Y. Z. Ider, "Convection-reaction equation based magnetic resonance electrical properties tomography (cr-mrept)," *IEEE Transactions on Medical Imaging*, vol. 33, no. 3, p. 777–793, 2014.

[22] J. Liu, X. ZNov hang4, S. Schmitter, P. van de Moortele, B. He, "Gradient-Based Electrical Properties Tomography (gEPT): A Robust Method for Mapping Electrical Properties of Biological Tissues In Vivo Using Magnetic Resonance Imaging," *Magnetic Resonance in Medicine*, vol. 74, no. 3, p. 634–646, 2015.

[23] E. Balidemaj, C. A. V. D. Berg, J. Trinks, A. L. V. Lier, A. J. Nederveen, L. J. A. Stalpers, H. Crezee, and R. F. Remis, "Csi-ept: A contrast source inversion approach for improved mri-based electric properties tomography," *IEEE Transa-cti ons on Medical Imaging*, vol. p34, no. 9, p. 788–796, 2015.

[24] U. Katscher, D. H. Kim, and J. K. Seo, "Recent Progress and Future Challenges in MR Electric Properties Tomography," *Computational and Mathematical Methods in Medicine*, vol. 2013, p. 1–11, 2013.

[25] N. Gurler and Y. Z. Ider, "Gradient-based electrical conductivity imaging using MR phase," *Magnetic Resonance in Medicine*, vol. 77, p. 137–150, 2016.

[26] C. Li, W. Yu and S. Y. Huang "An MR-Based Viscosity-Type Regularization Method for Electrical Property Tomography," *Tomography*, vol. 1, p. 50-59, 2017.

[27] G. Ariturk and Y. Z. Ider, "Optimal multichannel transmission for improved cr-MREPT," *Physics in Medicine and Biology*, vol. 63, p. 1-15, 2018.

[28] G. Yildiz and Y. Z. Ider, "Use of dielectric padding to eliminate low convective field artifact in cr-MREPT conductivity images," *Magnetic Resonance in Medicine*, vol. 81, p. 3168-3184, 2019.

[29] H. Ammari, H. Perreard, A. Kwon, Y. Lee, K. Kang and J. K. Seo, "Magnetic resonance-based reconstruction method of conductivit,y and permittivity distributions at the Larmor frequency," no. 1-4,*Inverse Problems*, vol. 31, p. 1-24, 2015.

[30] V. B. S. Prasath, D. Vorotnikov, R. Pelapur, S. Jose, G. Seetharaman and K. Palaniapan, "Multiscale Tikhonov-Total Variation Image Restoration Using Spatially Varying Edge Coherence Exponent," *IEEE Transactions on Image Processing*, vol. 24, p. 5220-5235, 2015.

[31] T. F. Chan, G. H. Golub and P. Mulet, "A Nonlinear Primal-Dual Method for Total Variation-Based Image Restoration," *SIAM Journal on Scientific Computing*, vol. 20, p. 1964-1977, 1999.

[32] L. I. Rudin, S. Osher and E. Fatemi, "Nonlinear total variation based noise removal algorithms," *Physica D: Nonlinear Phenomena*, vol. 60, p. 259-268, 1999.

[33] A. Borsic, B. M. Graham, A. Adler and W. R. B. Lionheart, "In Vivo Impedance Imaging With Total Variation Regularization," *IEEE Transactions on Medical Imaging*, vol. 29, p. 44-54, 2010.

[34] A. Borsic, I. M. Perreard, A. Mahara and W. R. J. Halter, "An Inverse Problems Approach to MR-EPT Image Reconstruction," *IEEE Transactions on Medical Imaging*, vol. 35, p. 244-256, 2016.

[35] N. Gurler and Y. Z. Ider, "Numerical methods and software tools for simulation, design, and resonant mode analysis of radio frequency birdcage coils used in MRI," vol. 45B, p. 13-32, 2015.